The extrudate swell singularity of Phan-Thien–Tanner and Giesekus fluids

Jonathan D. Evans[a], Morgan L. Evans[a]

[a] *Department of Mathematical Sciences, University of Bath, Bath, BA2 7AY*

Abstract

The stress singularity for Phan-Thien–Tanner (PTT) and Giesekus viscoelastic fluids is determined for extrudate swell (also termed die swell). In the presence of a Newtonian solvent viscosity, the solvent stress dominates the polymer stresses local to the contact point between the solid (no-slip) surface inside the die and the free (slip) surface outside the die. The velocity field thus vanishes like r^{λ_0}, where r is the radial distance from the contact point and λ_0 is the smallest Newtonian eigenvalue (dependent upon the angle of separation between the solid and free surfaces). The solvent stress thus behaves like $r^{-(1-\lambda_0)}$ and dominates the polymer stresses, which are like $r^{-4(1-\lambda_0)/(5+\lambda_0)}$ for PTT and $r^{-(1-\lambda_0)(3-\lambda_0)/4}$ for Giesekus. The polymer stresses require boundary layers at both the solid and free surfaces, the thicknesses of which are derived. These results do not hold for the Oldroyd-B fluid.

Keywords: Extrudate swell, singularity, viscoelastic, polymer

1. Introduction

Extrudate swell or "die swell", is a commonly encountered phenomenon in the polymer processing industry. It occurs in the extrusion of polymer melts or solutions, which are forced through an orifice or die into air. The die can typically be a thin plate (slit) or circular tube, and the resulting liquid stream generally attains its greatest cross-sectional area a few die-diameters downstream of the exit. Applications include pipe and profile extrusion [1], used in the production of rods, pipes and sheets. Once the fluid emerges from the die, it exhibits the characteristic phenomenon called "extrudate swell" or "jet swell". As a quantitative measure of the swelling behaviour, it is most commonly given as the ratio or percentage change of the extrudate dimension to the die dimension. Precision extrusion requires the accurate prediction of the swelling, but it is also of intrinsic interest to understand its mechanism. The extrusion process is thus of technological interest and remains a challenging problem both analytically and numerically, due to the presence of a free surface and a stress singularity at the die lip.

In discussion of the extrudate swell phenomenon it is convenient to consider an infinite jet with no downstream influences. The downstream conditions tend not to influence the final swelling ratio, only the distance from the die exit at which it is attained. For example, gravity is often ignored and there is assumed to be an absence of axial tension (as would arise, for example, from a take-up spool). In contrast, upstream conditions can strongly influence the swelling ratio, which is highly dependent on the die length. In short dies, flow never reaches the fully developed state and the exit dynamics become dependent on the inlet conditions. However, it is usual to consider an infinitely long die, for which the exit dynamics are independent of the inlet conditions. For a given polymer in a given geometry the swelling ratio generally increases with flow rate up to a maximum where the flow becomes unstable and melt fracture occurs [2, 3]. Another influence of the swelling ratio is the type of polymer material. Newtonian jets

Email addresses: masjde@bath.ac.uk (Jonathan D. Evans), M.L.Evans@bath.ac.uk (Morgan L. Evans)

tend to expand for low Reynolds numbers $Re < 16$ and contract for $Re > 16$. The swelling ratio being typically 1.1 to 1.2 for low Reynolds numbers and reduces to $\sqrt{3}/2 \approx 0.866$ for high Reynolds numbers $Re > 150$ [4, 5, 6, 7, 8] (this value being insensitive for higher Reynolds numbers). The expansion effects at low Reynolds numbers are far larger for viscoelastic jets, where the swelling ratios can between 2 and 3 [9, 10, 11].

Approaches to solve the extrudate swell problem have mainly fallen into the categories of analytical or numerical. The number of exact analytical solutions to the problem remains small. Stick-slip is the linearised version of extrudate swell in which the free surface remains a direct continuation of the die wall and arises in the large surface tension limit. The planar Stokes flow case was solved by Richardson [12] using the Wiener-Hopf technique, with the strength of the singularity corrected by Tanner & Huang [13], whilst Sturges [14] corrected the eigenfunction expansion originally attempted by Zidan [15]. Trogdon and Joseph [16] used both methods for the round jet in the axisymmetric case. Coleman [17] demonstrated that Richardson's solution was relevant to a second-order fluid, whilst Sturges [18] extended the approach to simple fluids described by Rivlin-Ericksen tensors. Other than this, very little progress has been made analytically with viscoelastic models.

Closely allied to the analytical approach, are the use of global integral balances of mass and momentum to predict the final swelling ratio and to determine normal stress measurements experimentally. Harmon [4] first used this approach to predict the final diameter of Newtonian jets at high Reynolds numbers, with subsequent adjustments for Newtonian jets [19, 5, 20, 21] and non-Newtonian jets [21, 22, 5, 23, 24, 25, 26, 27, 28] at low Reynolds numbers. The main drawback in the arguments used is the assumption of fully-developed viscometric flow holding up to the die exit, as well as simplification of the pressure field at that location. As a consequence, the theoretical estimates fail to agree quantitatively with experimental data, particularly in the low Reynolds number regime. The use of exit flow measurements to determine normal stress measurements is critically examined in Boger and Denn [27] and illustrates the failings of the approach for viscoelastic fluids without a suitable knowledge of the exit velocity profiles.

Numerical simulation of extrudate swell for Newtonian jets were successful early on in both the low and high Reynolds number regimes [29, 30, 31, 32, 33, 34, 35]. The approaches were predominately finite-element and solutions agreed well with experiments. However, the same methodology had less initial success for non-Newtonian fluids. Crochet and Keunings [32, 36] first successfully simulated extrudate swell for the upper-convected Maxwell and Oldroyd-B fluids upto moderate elasticity numbers (as measured by Weissenberg or Deborah numbers) for slit and circular dies using a mixed finite-element scheme with a conformal mapping of the mesh onto a fixed Cartesian grid. However, the simulations were well below elasticity numbers for which dramatic viscoelastic effects have been observed experimentally. This work has been extended by many authors to higher Weissenberg/Deborah numbers and other differential and integral viscoelastic constitutive models. Techniques are predominately finite-element [37, 38, 39, 40, 41], although spectral elements have also been successfully implemented [42, 43], as well as arbitrary-Langrangian-Eulerian methods [44, 45] and mesh-free smoothed particle hydrodynamics [46, 47, 48]. Finite-difference schemes have been implemented in an explicit front-tracking marker-and-cell method for Oldroyd-B, Phan-Thien–Tanner, Giesekus, Pom-Pom and KBKZ type viscoelastic models [49, 50, 51, 52, 53, 54, 55, 56]. Volume-of-fluid methods follow the free-surface implicitly through a colour function and have been successfully implemented for Oldoyd-B and Giesekus models in OpenFOAM [57, 58].

As remarked upon by several authors [59, 60, 61, 62], a good understanding of the extrudate swell phenomenon requires knowledge of the singularity at the join of the die wall and free-surface. This has been lacking so far for all of the viscoelastic fluid models possessing memory. We present here the stress singularities relevant to the Phan-Thien–Tanner [63, 64] and Giesekus [65] models. The origin of the stress singularity is due to sudden change in boundary conditions along the die wall of no-slip to those of stress-free conditions on the emerging free-surface. These

mixed boundary conditions lead naturally to singular behaviour in the velocity gradients and polymer stresses. For Newtonian liquids, this stress singularity was determined by Michael [66] and later Moffatt [67], and used in the analytical solution of stick-slip by Richardson [12] and Trogdon and Joseph [16]. Knowledge of the singularity is also important for numerical schemes by improving their convergence around such points and clearly demonstrated in the work of Georgiou et al. [68, 69] and Elliotis et al. [70] for Newtonian viscous fluids. For viscoelastic fluids however, limited success has been achieved in understanding the singularity. The work of Salamon et al. [71] for the Oldroyd-B fluid relaxed the no-slip condition on the die wall and in the stick-slip situation were then able to derive a logarithmic behaviour for stress with wall slip present. This behaviour however is lost as wall slip is reduced and sheds no light on the no-slip wall situation.

In the analysis we present here, the Phan-Thien–Tanner and Giesekus models share a common feature of possessing quadratic stress terms in their constitutive equations. This property allows these models to not only capture shear-thinning effects exhibited by many real polymers, but crucially allows the solvent stresses to dominate the polymer stresses at the singularity. As such, the flow field is locally Newtonian and it is this fact that we exploit to extract the solvent and polymer stress behaviours. The results presented here, extend those of stick-slip in [72, 73, 74] to more general separation angles relevant to extrudate swell.

The layout of the paper is as follows. The geometry and equations for the extrudate swell problem are given in section 2. The main results are then derived in section 3, where the asymptotic arguments are given for the polymer stresses in polar form and the stress singularity is determined. The corresponding results for the natural stress variables are then given in section 4. In section 5 we confirm our analytical results by solving the equations studied in sections 3 and 4 numerically. Finally, in section 6, we confirm convergence of a full numerical simulation of the extrudate swell problem to the derived theoretical singular behaviour at the die-edge contact point.

2. The extrudate swell problem

We consider a jet emerging from a slit die, in the absence of gravity, as sketched in Figure 1. The fluid density ρ is assumed constant, due to the absence of large pressures required to give density changes for polymeric fluids and the normally negligible temperature variations. We assume fully developed Poiseuille flow within the die and that downstream outside the die, plug flow is eventually reached. For the steady-state, planar, incompressible extrudate swell problem of viscoelastic fluids, the continuity and equation of motion are written as

$$\nabla \cdot \mathbf{u} = 0, \qquad \rho(\mathbf{u} \cdot \nabla)\mathbf{u} = -\nabla p + \nabla \cdot \boldsymbol{\tau}, \tag{1}$$

for velocity $\mathbf{u}$, pressure p, fluid density ρ and $\boldsymbol{\tau}$ the extra-stress tensor. As constitutive equations we adopt the PTT (the affine and linear stress function versions) and Giesekus models in the presence of a Newtonian solvent, for which

$$\boldsymbol{\tau} = \boldsymbol{\tau}^s + \boldsymbol{\tau}^p, \tag{2}$$

where $\boldsymbol{\tau}^s = 2\eta_s \mathbf{D}$ is the Newtonian solvent stress and the polymeric stress is given by

$$\boldsymbol{\tau}^p + \lambda_p \left(\overset{\triangledown}{\boldsymbol{\tau}}^p + \kappa \mathbf{g}(\boldsymbol{\tau}^p) \right) = 2\eta_p \mathbf{D}. \tag{3}$$

Here $\mathbf{D} = \frac{1}{2}\left(\nabla\mathbf{u} + (\nabla\mathbf{u})^T\right)$ is the rate-of-deformation tensor, λ_p the relaxation time, $\overset{\triangledown}{\boldsymbol{\tau}}^p$ the upper-convected derivative of the polymeric extra-stress, η_s the solvent viscosity and η_p the polymeric viscosity. The model dependent quadratic stress term is

$$\mathbf{g}(\boldsymbol{\tau}^p) = \begin{cases} (\operatorname{tr}\boldsymbol{\tau}^p)\boldsymbol{\tau}^p, & \text{PTT}, \\ (\boldsymbol{\tau}^p)^2, & \text{Giesekus}, \end{cases} \tag{4}$$

(a)

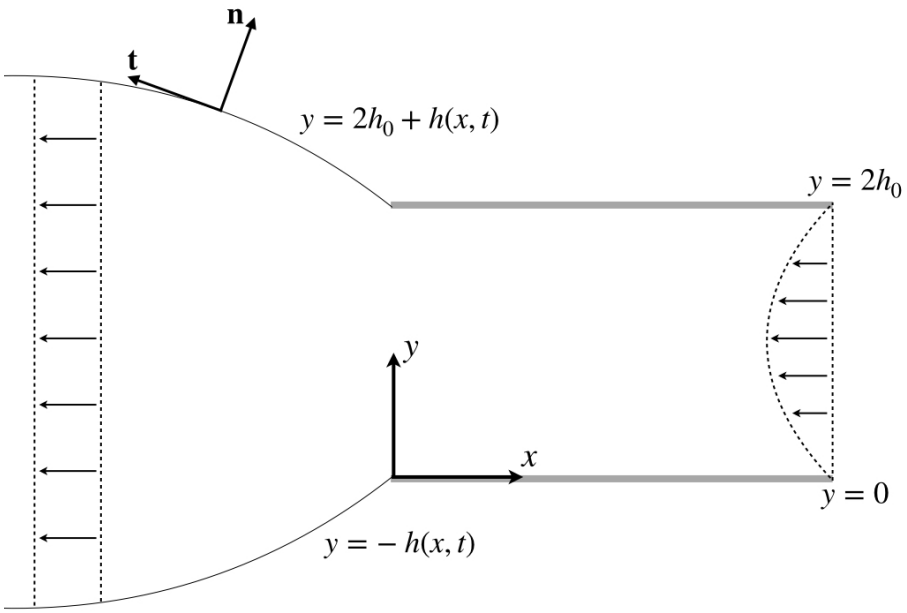

(b)

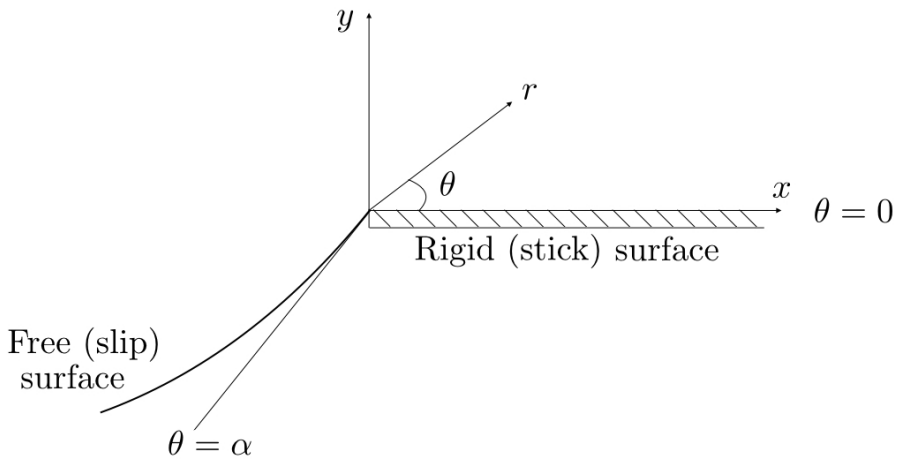

Figure 1: (a) Fluid flow through the die from right to left. The walls of the die are $y = 0, 2h_0$ with $x > 0$, and the free surface $y = 2h_0 + h(x,t), -h(x,t)$ with $x < 0$. (b) A local coordinate system located at the lower half of the die exit. The die wall is at $\theta = 0$ and the free surface at $\theta = \alpha$ with $r \ll 1$.

with the common model dependent parameter κ being often termed ϵ for PTT and the mobility factor α for Giesekus.

On the solid wall of the die the fluid satisfies the no-slip condition

$$\mathbf{u} = 0, \tag{5}$$

whilst on the free surface of the jet, the normal component of the velocity and the shear stress vanish

$$\mathbf{u} \cdot \mathbf{n} = 0, \qquad \boldsymbol{\tau}_{nt} = 0, \tag{6}$$

($\mathbf{n}$ being the outward unit normal) and the jump in normal stress is balanced by surface tension

$$\boldsymbol{\tau}_{nn} - p + p_a = \sigma \mathcal{K}, \tag{7}$$

p_a is the external atmospheric pressure, σ is the surface tension and $\mathcal{K}$ is the mean curvature of the jet boundary.

We non-dimensionalise using the channel half-width h_0 and characteristic velocity U (defined as the average flow velocity) of the fully developed channel inlet flow. Thus

$$\begin{aligned} &\mathbf{x} = h_0 \mathbf{x}^*, \quad h = h_0 h^*, \quad \mathbf{u} = U \mathbf{u}^*, \quad p = \frac{\eta_0 U}{h_0} p^*, \quad p_a = \frac{\eta_0 U}{h_0} p_a^*, \\ &\boldsymbol{\tau}^s = \frac{\eta_s U}{h_0} \mathbf{T}^{s*}, \quad \boldsymbol{\tau}^p = \frac{\eta_p U}{h_0} \mathbf{T}^{p*}, \quad \boldsymbol{\tau} = \frac{\eta_0 U}{h_0} \mathbf{T}^*, \end{aligned} \tag{8}$$

give (upon dropping *'s) the dimensionless governing equations

$$\nabla \cdot \mathbf{u} = 0, \qquad \mathbf{0} = -\nabla p + \nabla \cdot \mathbf{T}, \tag{9}$$

where

$$\mathbf{T} = \beta \mathbf{T}^s + (1 - \beta) \mathbf{T}^p, \tag{10}$$

with

$$\mathbf{T}^s = 2\mathbf{D}, \qquad \mathbf{T}^p + \mathrm{Wi} \left(\overset{\triangledown}{\mathbf{T}}^p + \kappa \mathbf{g}(\mathbf{T}^p) \right) = 2\mathbf{D}, \tag{11}$$

the Weissenberg number Wi being $\lambda_p U / h_0$, $\eta_0 = \eta_s + \eta_p$ the zero shear (or total) viscosity and $\beta = \eta_s / \eta_0$ the solvent viscosity fraction. The die walls are now at $y = 0, 2$ at which (5) holds, whilst on the free surfaces $y = -h(x,t)$ and $y = 2 + h(x,t)$, (6) and (7) become

$$\mathbf{u} \cdot \mathbf{n} = 0, \qquad T_{nt} = 0, \qquad T_{nn} = p - p_a + \frac{\mathcal{K}}{C_a}, \tag{12}$$

where $C_a = \eta_0 U / \sigma$ is the capillary number.

We are interested in examining these equations locally at the die exit, as depicted in Figure 1(b). Consequently there is no length scale attached to the problem and as a result, we may set the Weissenberg number to unity (without loss of generality). The inertia term may also be neglected in the momentum equation (9) since it can be shown a posteriori to be uniformly sub-dominant. We take a local coordinate system fixed at the exit on the lower die wall and consider the sector $0 < r < \infty$, $0 < \theta < \alpha$, where the separation angle α of the free (slip) surface lies between $\pi/2$ and $3\pi/2$. In the analysis we present, the separation angle enters as a parameter. It cannot be determined through a local analysis alone, since the jet surface is not plane. As discussed by Sturges [14], the normal stress condition in (12) is not imposed, but rather used to determine the free-surface curvature once velocity and stresses are determined, with global flow behaviour then determining the separation angle. As surface tension only enters the normal stress condition, its effect thus enters indirectly on the singularity by influencing the resulting separation angle.

3. Asymptotics

We seek to describe the asymptotic behaviour of the velocity and stresses near to the die exit location at the wall. This is at the trijunction of two immiscible fluids and a solid, and represents a three-phase contact line problem at the die edge. The mathematical singularities introduced at such points are discussed in Salamon et al. [75] for the Newtonian case. This will turn out to be relevant to providing the behaviour of the velocity field and consequently the solvent stress. However, the asymptotics for the polymer stress is more involved, requiring in addition separate boundary layers at both the die wall no-slip surface as well as the free slip surface.

The starting point of the analysis is the a priori assumption that the solvent stress dominates the polymer stress in a region close to the contact point singularity. This will turn out to be the case for both PTT and Giesekus models, holding close to the die edge, but away from both the solid and free surfaces. Thus, we assume

$$(1-\beta)\mathbf{T}^p \ll \beta\mathbf{T}^s \qquad \text{as } r \to 0, \tag{13}$$

where both solvent and polymer stresses possess singular behaviour. This gives a Newtonian balance $\mathbf{T} \sim \beta\mathbf{T}^s$ for the total extra-stress, and the momentum equation reduces to the Stokes flow equation

$$\mathbf{0} = -\nabla p + \beta\nabla^2\mathbf{u}. \tag{14}$$

Well known separable solutions are recorded in [66], [67] and [14]. Using a streamfunction representation for the velocity, we can write the solutions as

$$\psi = \frac{C_0 r^{\lambda_0+1}}{\lambda_0}\left(\sin(\lambda_0\theta)\sin(\theta) - B_\alpha\left[\sin(\lambda_0\theta)\cos(\theta) - \lambda_0\cos(\lambda_0\theta)\sin(\theta)\right]\right), \tag{15}$$

$$p = 2\beta C_0 r^{\lambda_0-1}\left(\sin((1-\lambda_0)\theta) - B_\alpha\left(\lambda_0+1\right)\cos((1-\lambda_0)\theta)\right), \tag{16}$$

with the constant

$$B_\alpha = \frac{\sin(\lambda_0\alpha)\sin(\alpha)}{\sin(\lambda_0\alpha)\cos(\alpha) - \lambda_0\cos(\lambda_0\alpha)\sin(\alpha)} \tag{17}$$

and the relationship between the eigenvalue λ_0 and separation angle α being given by the transcendental equation

$$\lambda_0\sin(2\alpha) - \sin(2\lambda_0\alpha) = 0. \tag{18}$$

A discussion of the eigenvalues to (18) is given in Lugt & Schwiderski [76]. A countable set

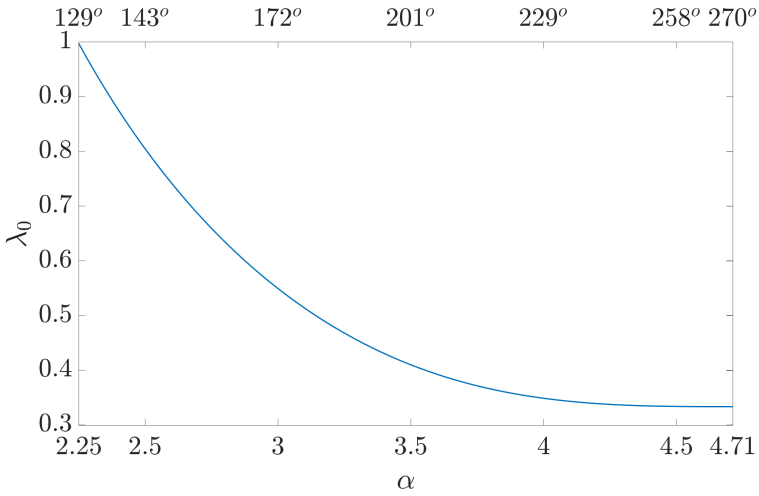

Figure 2: A plot of the relationship between the separation angle α and the lead eigenvalue λ_0.

exits, with the smallest one being the most relevant for our asymptotics, a succinct summary of the properties of which is given in Sturges [14]. For $\alpha < \alpha_1 \approx 78^o$, the first eigenvalue is complex, whilst for $\alpha_1 < \alpha < \alpha_2 \approx 129^o$ it is real but greater than 1. Consequently for $\alpha < \alpha_2$, the velocity gradients and pressure are not singular. For $\alpha_2 < \alpha < 270^o$ the first eigenvalue is real and lies in the range $1/3 < \lambda_0 < 1$. Its behaviour is plotted in Figure 2, showing that it decreases monotonically to $1/3$ as α increases to 270^o or $3\pi/2$.

The arbitrary constant C_0 in expressions (15)–(16) is determined globally by flow away from the separation point. Its sign determines the direction of flow. This Newtonian flow field gives the order of magnitude estimates

$$\mathbf{u} = O(r^{\lambda_0}), \quad \nabla\mathbf{u} = O(r^{-(1-\lambda_0)}), \quad \mathbf{T}^s = O(r^{-(1-\lambda_0)}) \qquad \text{as } r \to 0. \tag{19}$$

Using these along with the assumption in (13) implies the dominance of the upper convected derivative in the polymeric stress equation (11) resulting in

$$\overset{\triangledown}{\mathbf{T}}{}^p = 0 \qquad \text{as } r \to 0. \tag{20}$$

A particular well known stretching solution to (20), see Hinch [77], takes the form

$$\mathbf{T}^p = \lambda(\psi)\,\mathbf{u}\mathbf{u}^T, \tag{21}$$

where the function $\lambda(\psi)$ is constant along streamlines. As we will see later, the viscometric behaviour of the polymer stresses near the solid no-slip die wall, suggest a power law form for this dependence, which we take in the form

$$\lambda(\psi) = C_1 \left(\frac{\psi}{C_0}\right)^{n_1}, \tag{22}$$

introducing an arbitrary constant C_1 and unknown exponent n_1. The viscometric region near the die wall forms a separate asymptotic region, in which the assumption (13) does not hold as the polymer and solvent stresses will be shown to have comparable size. We will derive the dependencies of the exponent on the eigenvalue for the two models as

$$n_1 = \begin{cases} -\frac{2(\lambda_0+2)}{\lambda_0+5}, & \text{PTT,} \\ -\frac{\lambda_0+3}{4}, & \text{Giesekus,} \end{cases} \tag{23}$$

from which we may deduce

$$\mathbf{T}^p = \begin{cases} O(r^{-\frac{4(1-\lambda_0)}{\lambda_0+5}}), & \text{PTT,} \\ O(r^{-\frac{(1-\lambda_0)(3-\lambda_0)}{4}}), & \text{Giesekus} \end{cases} \qquad \text{as } r \to 0. \tag{24}$$

The assumption (13) is satisfied for both models when $\lambda_0 < 1$, which holds for all separation angles of interest to extrudate swell from 129^o upto 270^o. These estimates breakdown in the absence of a solvent viscosity and thus are restricted to the parameter range $0 < \beta \leq 1$. Further, the presence of the quadratic stress terms is also crucial, so that the model parameter $\kappa > 0$.

To derive the results (24), it is convenient to use polar coordinates and consider the constitutive equations posed along streamlines. As such, we write the streamfunction (15) in the form

$$\psi = C_0 r^{\lambda_0+1} f(\theta), \tag{25}$$

so that the velocity components are given by

$$u_r = \frac{1}{r}\frac{\partial\psi}{\partial\theta} = C_0 r^{\lambda_0} f'(\theta), \qquad u_\theta = -\frac{\partial\psi}{\partial r} = -C_0(\lambda_0+1) r^{\lambda_0} f(\theta). \tag{26}$$

In polar coordinates the component form of the polymeric constitutive equations (11) may be written as

$$\begin{aligned}
&T^p_{rr} + (\mathbf{u}\cdot\nabla)T^p_{rr} - 2\frac{\partial u_r}{\partial r}T^p_{rr} - \frac{2}{r}\frac{\partial u_r}{\partial \theta}T^p_{r\theta} + \kappa g_{rr} = 2\frac{\partial u_r}{\partial r},\\
&T^p_{r\theta} + (\mathbf{u}\cdot\nabla)T^p_{r\theta} + \frac{u_\theta}{r}T^p_{rr} - \frac{1}{r}\frac{\partial u_r}{\partial \theta}T^p_{\theta\theta} - \frac{\partial u_\theta}{\partial r}T^p_{rr} + \kappa g_{r\theta} = \frac{1}{r}\frac{\partial u_r}{\partial \theta} - \frac{u_\theta}{r} + \frac{\partial u_\theta}{\partial r},\\
&T^p_{\theta\theta} + (\mathbf{u}\cdot\nabla)T^p_{\theta\theta} + 2\frac{u_\theta}{r}T^p_{r\theta} - 2\frac{\partial u_\theta}{\partial r}T^p_{r\theta} - \frac{2}{r}\frac{\partial u_\theta}{\partial \theta}T^p_{\theta\theta} - 2\frac{u_r}{r}T^p_{\theta\theta} + \kappa g_{\theta\theta} = 2\left(\frac{1}{r}\frac{\partial u_\theta}{\partial \theta} + \frac{u_r}{r}\right),
\end{aligned} \tag{27}$$

where

$$\begin{aligned}
g_{rr} &= \begin{cases} (T^p_{rr} + T^p_{\theta\theta})T^p_{rr}, & \text{PTT},\\ (T^p_{rr})^2 + (T^p_{r\theta})^2, & \text{Giesekus}, \end{cases}\\
g_{r\theta} &= (T^p_{rr} + T^p_{\theta\theta})T^p_{r\theta}, \qquad \text{PTT \& Giesekus},\\
g_{\theta\theta} &= \begin{cases} (T^p_{rr} + T^p_{\theta\theta})T^p_{\theta\theta}, & \text{PTT},\\ (T^p_{r\theta})^2 + (T^p_{\theta\theta})^2, & \text{Giesekus}. \end{cases}
\end{aligned} \tag{28}$$

Streamlines are level curves of the streamfunction (25) which consequently (by eliminating the appropriate variable) allows parameterisation by either the polar angle or radial distance. Along streamlines $\frac{1}{r}\frac{dr}{d\theta} = \frac{u_r}{u_\theta}$, so that the derivative along a streamline $\mathbf{u}\cdot\nabla$ can be expressed as a total derivative $\frac{u_\theta}{r}\frac{d}{d\theta}$ for the θ parameterisation or $u_r\frac{d}{dr}$ for the r parameterisation. Consequently, for either parameterisation, the polymeric stress equations (11) reduce to a system of ordinary differential equations (ODEs). Along any given streamline, the minimum radial distance from the contact point singularity occurs when $f'(\theta) = 0$, allowing both the angle θ_{min} and distance r_{min} at which this occurs to be calculated. Figure 3 gives these values for selected streamlines that pass close to the die edge singularity.

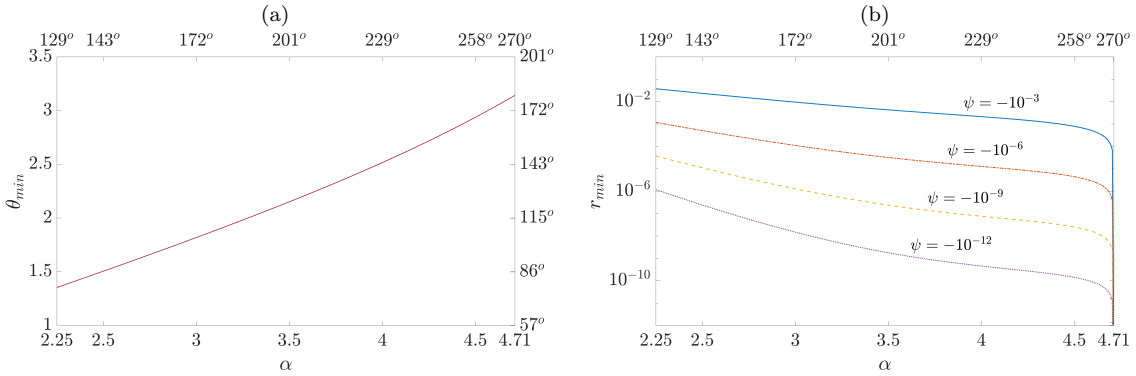

Figure 3: The behaviour of (a) θ_{min} against α, and (b) r_{min} against α.

3.1. The wall boundary layer

We begin by considering the region close to the no-slip die wall, where θ is small. At leading order in θ, the streamfunction and velocity components are

$$\psi \sim C_0 r^{\lambda_0+1}\theta^2, \qquad u_r \sim 2C_0 r^{\lambda_0}\theta, \qquad u_\theta \sim -(\lambda_0+1)C_0 r^{\lambda_0}\theta^2 \qquad \text{as } \theta \to 0. \tag{29}$$

Useful to our discussion are two components of the velocity gradient, namely the radial strain-rate $\dot{e}$ and the shear rate $\dot{\gamma}$, which in this region take the form

$$\dot{e} = \frac{\partial u_r}{\partial r} \sim 2\lambda_0 C_0 r^{\lambda_0-1}\theta, \qquad \dot{\gamma} = \frac{1}{r}\frac{\partial u_r}{\partial \theta} \sim 2C_0 r^{\lambda_0-1}. \tag{30}$$

Viscometric polymer stresses are those given by steady simple shear and satisfy

$$T^p_{rr} - 2\dot\gamma T^p_{r\theta} + \kappa g_{rr} = 0, \quad T^p_{r\theta} - \dot\gamma T_{\theta\theta} + \kappa g_{r\theta} = \dot\gamma, \quad T^p_{\theta\theta} + \kappa g_{\theta\theta} = 0, \tag{31}$$

where $\dot\gamma$ is often termed the wall shear rate. These follow from (27) for small theta with the shear rate as in (30). Since we are interested in small radial distances, the shear rate is large, so that (31) simplify. For $|\dot\gamma| \gg 1$, the PTT viscometric behaviour is

$$T^p_{rr} \sim 2\left(\frac{\dot\gamma}{2\kappa}\right)^{\frac{2}{3}}, \qquad T^p_{r\theta} \sim \left(\frac{\dot\gamma}{2\kappa}\right)^{\frac{1}{3}}, \qquad T^p_{\theta\theta} = 0, \tag{32}$$

and for Giesekus

$$T^p_{rr} \sim \left(\frac{2|\dot\gamma|}{\kappa}\right)^{\frac{1}{2}} a^{\frac{1}{2}}, \quad T^p_{r\theta} \sim -a, \quad T^p_{\theta\theta} \sim -1 + \left(\frac{2\kappa}{|\dot\gamma|}\right)^{\frac{1}{2}} a^{\frac{3}{2}}, \tag{33}$$

where

$$a = \left(\frac{1-\kappa}{\kappa}\right)^{\frac{1}{2}}. \tag{34}$$

The next step is to determine when these behaviours break down. Focusing on the equation for the largest and most important stress component T^p_{rr}, the first equation in (27) can be written in the form

$$T^p_{rr} + (\mathbf{u}\cdot\nabla)T^p_{rr} - 2\dot e T^p_{rr} - 2\dot\gamma T^p_{r\theta} + \kappa g_{rr} = 2\dot e.$$

In order to transition to the stretching behaviour region, terms in the upper convected derivative should have comparable size, so that

$$\dot e T^p_{rr} = O(\dot\gamma T^p_{r\theta}). \tag{35}$$

Using the viscometric polymer stress functions in (32) and (33) we have at viscometric breakdown

$$\begin{aligned} \text{PTT:}\ \ \dot e &= O(\dot\gamma^{\frac{2}{3}}), \\ \text{Giesekus:}\ \ \dot e &= O(|\dot\gamma|^{\frac{1}{2}}). \end{aligned} \tag{36}$$

Using (30) then gives the estimates

$$\theta = O(r^n), \qquad n = \begin{cases} \frac{1-\lambda_0}{3}, & \text{PTT}, \\ \frac{1-\lambda_0}{2}, & \text{Giesekus}, \end{cases} \tag{37}$$

as the extent of the viscometric region at the wall. This region is asymptotically thin and may be termed the wall boundary layer for the polymer stress. We note that at the top of the boundary layer, the streamfunction in (29) together with (37) give the following estimates

$$r = O(\left(\frac{\psi}{C_0}\right)^{\frac{1}{2n+\lambda_0+1}}), \qquad \theta = O(\left(\frac{\psi}{C_0}\right)^{\frac{n}{2n+\lambda_0+1}}), \tag{38}$$

for the location of the viscometric break down along a given streamline. The values of the radial velocity component and shear rate in (29) and (30) are then

$$u_r = O(\left(\frac{\psi}{C_0}\right)^{\frac{n+\lambda_0}{2n+\lambda_0+1}}), \qquad \dot\gamma = O(\left(\frac{\psi}{C_0}\right)^{\frac{\lambda_0-1}{2n+\lambda_0+1}}), \tag{39}$$

for use in section 3.2. As θ increases we move into the polymer stretching region, which we now address.

3.2. Stretching behaviour away from the surfaces

We have already noted that, away from the wall and free surface, but close to the contact point, the upper convected stress terms dominate in the constitutive equations. This is a consequence of assuming that the velocity gradients are more singular than the polymer stresses, as in (13). The polymeric constitutive equations thus reduce to (20), which possess the stretching solution (21). Within this solution the scalar function λ, which is constant along streamlines, needs to be determined. This may be done by matching the limiting behaviours of the largest polymer stress component, namely the normal radial component T^p_{rr}. At viscometric break down, the limiting behaviour of the stretching solution, $T^p_{rr} = \lambda(\psi)u_r^2$ must agree with its model dependent viscometric behaviour in (32) or (33). Using (39) in these expressions, gives (22) with (23), where C_1 is an arbitrary constant and the all important variation across streamlines has been determined in power law form. As a result, the singular polymer stress behaviours (24) may be determined for this region and for later reference, the polar components are

$$T^p_{rr} = \lambda(\psi)u_r^2, \quad T^p_{r\theta} = \lambda(\psi)u_r u_\theta, \quad T_{\theta\theta} = \lambda(\psi)u_\theta^2, \tag{40}$$

with the velocity components as given in (26).

3.3. The slip surface boundary layer

Near the slip surface we have that $\theta \approx \alpha$, resulting in the following behaviours for the streamfunction and velocity components

$$\psi \sim C_0 C_\alpha r^{\lambda_0+1}(\alpha-\theta), \quad u_r \sim -C_0 C_\alpha r^{\lambda_0}, \quad u_\theta \sim -(\lambda_0+1)C_0 C_\alpha r^{\lambda_0}(\alpha-\theta), \tag{41}$$

where

$$C_\alpha = \frac{1}{\lambda_0}\frac{(\lambda_0\sin(\alpha)+\sin(\lambda_0\alpha))\,(\lambda_0\sin(\alpha)-\sin(\lambda_0\alpha))}{\sin(\lambda_0\alpha)\cos(\alpha)-\lambda_0\cos(\lambda_0\alpha)\sin(\alpha)}.$$

The radial strain rate is

$$\dot{e} \sim -\lambda_0 C_0 C_\alpha r^{\lambda_0-1}, \tag{42}$$

with a vanishingly small shear rate $\dot{\gamma} = o(1)$, implying the dominance of elongational flow in this region as expected. Using the radial distance to parameterise streamlines, we have the following limiting behaviours of the stretching solution (40)

$$\begin{aligned} T^p_{rr} &\sim C_\alpha^2 C_0^2 C_1 \left(\frac{\psi}{C_0}\right)^{n_1} r^{2\lambda_0}, \\ T^p_{r\theta} &\sim (\lambda_0+1)C_\alpha C_0^2 C_1 \left(\frac{\psi}{C_0}\right)^{n_1+1} r^{\lambda_0-1}, \\ T_{\theta\theta} &\sim (\lambda_0+1)^2 C_0^2 C_1 \left(\frac{\psi}{C_0}\right)^{n_1+2} r^{-2}, \end{aligned} \tag{43}$$

as the slip surface region is approached. Again, the normal radial stress component T^p_{rr} is the largest and now grows with respect to radial distance whilst the remaining components decay. Focussing on the first equation in (27) for T^p_{rr}, we write it as

$$T^p_{rr} + (\mathbf{u}\cdot\nabla)T^p_{rr} - 2\dot{e}T^p_{rr} - \dot{\gamma}T^p_{r\theta} + \kappa g_{rr} = 2\dot{e}. \tag{44}$$

Since the radial strain rate $\dot{e}$ is decreasing, whilst the normal radial stress T^p_{rr} is growing, eventually the leading order quadratic stress term enters the balance with the upper convective derivative terms. This occurs when

$$\kappa T^{p2}_{rr} = O(\dot{e}T^p_{rr}) \quad \text{or} \quad \kappa T^p_{rr} = O(\dot{e}) \tag{45}$$

and demarcates the edge of slip boundary layer. Using the expression for the streamfunction in (41), together with (42) and (43) in this relationship gives the estimates

$$(\alpha - \theta) = O(r^m), \qquad m = \begin{cases} \frac{(1-\lambda_0^2)}{2(\lambda_0+2)}, & \text{PTT}, \\ \frac{(1-\lambda_0^2)}{(\lambda_0+3)}, & \text{Giesekus}. \end{cases} \tag{46}$$

Within this region, equation (44) reduces to

$$r\frac{d}{dr}T^p_{rr} - 2\lambda_0 T^p_{rr} - \kappa\frac{r^{1-\lambda_0}}{C_0 C_\alpha}(T^p_{rr})^2 = 0, \tag{47}$$

on keeping the leading order terms only. This has the exact solution

$$T^p_{rr} = \frac{C_\alpha^2 C_0^2 C_1 \left(\frac{\psi}{C_0}\right)^{n_1} r^{2\lambda_0}}{1 - \frac{\kappa}{(\lambda_0+1)} C_\alpha C_0 C_1 \left(\frac{\psi}{C_0}\right)^{n_1} r^{\lambda_0+1}}, \tag{48}$$

using (43) from the stretching region as the initial behaviour. Consequently, as r increases along the streamline, the growth of this stress component is arrested by the presence of the quadratic stress term. Another observation is that on the free-surface $\psi = 0$, (48) reduces to

$$T^p_{rr} = -\frac{(\lambda_0+1)}{\kappa} C_\alpha C_0 r^{\lambda_0 - 1}. \tag{49}$$

This value is finite for both PTT and Giesekus models when $\kappa > 0$, but in the Oldroyd-B limit $\kappa \to 0$, it blows up. We comment more on the Oldroyd-B case elsewhere.

This completes the discussion of the asymptotic regions, with the velocity and stress behaviours within them. The polymer stress requires boundary layers at both surfaces, although their structures are different and are linked through the stretching region in which the polymer convects and deforms affinely. Next, we provide complimentary analysis motivated by the form of the stretching solution (21).

4. Asymptotics for the natural stresses

In regions where the upper convected stress derivative dominates in the polymer equations, such as near stress singularities, it is beneficial to align the stress tensor along streamlines. Not only has it been shown to eliminate numerical instability [78], but also facilitates asymptotic matching between regions [79]. To do this, the polymer stress tensor is represented through the dyadic representation

$$\mathbf{T}^p = -\mathbf{I} + \lambda \mathbf{u}\mathbf{u}^T + \mu(\mathbf{u}\mathbf{w}^T + \mathbf{w}\mathbf{u}^T) + \nu \mathbf{w}\mathbf{w}^T, \tag{50}$$

using the velocity $\mathbf{u}$ and a perpendicular vector $\mathbf{w}$, taken to be

$$\mathbf{u} = (u_r, u_\theta)^T, \qquad \mathbf{w} = \left(-\frac{u_\theta}{u_r^2 + u_\theta^2}, \frac{u_r}{u_r^2 + u_\theta^2}\right)^T. \tag{51}$$

The components in (50) are referred to as the natural stress variables, and when used in the constitutive equations (11), give the component equations

$$\begin{aligned} &\lambda + (\mathbf{u}\cdot\nabla)\lambda + 2\mu(\nabla\cdot\mathbf{w}) + \kappa g_\lambda = \frac{1}{\|\mathbf{u}\|^2}, \\ &\mu + (\mathbf{u}\cdot\nabla)\mu + \nu(\nabla\cdot\mathbf{w}) + \kappa g_\mu = 0, \\ &\nu + (\mathbf{u}\cdot\nabla)\nu + \kappa g_\nu = \|\mathbf{u}\|^2, \end{aligned} \tag{52}$$

where

$$g_\lambda = \begin{cases} \left(\lambda\|\mathbf{u}\|^2 - 2 + \frac{\nu}{\|\mathbf{u}\|^2}\right)\left(\lambda - \frac{1}{\|\mathbf{u}\|^2}\right), & \text{PTT}, \\ \frac{\mu^2}{\|\mathbf{u}\|^2} + \left(\lambda\|\mathbf{u}\| - \frac{1}{\|\mathbf{u}\|}\right)^2, & \text{Giesekus}, \end{cases}$$

$$g_\mu = \left(\lambda\|\mathbf{u}\|^2 - 2 + \frac{\nu}{\|\mathbf{u}\|^2}\right)\mu, \qquad \text{PTT \& Giesekus}, \tag{53}$$

$$g_\nu = \begin{cases} \left(\lambda\|\mathbf{u}\|^2 - 2 + \frac{\nu}{\|\mathbf{u}\|^2}\right)\left(\nu - \|\mathbf{u}\|^2\right), & \text{PTT}, \\ \mu^2\|\mathbf{u}\|^2 + \left(\frac{\nu}{\|\mathbf{u}\|} - \|\mathbf{u}\|\right)^2, & \text{Giesekus} \end{cases}$$

and

$$\nabla\cdot\mathbf{w} = \frac{1}{\|\mathbf{u}\|^4}\left((u_\theta^2 - u_r^2)\left(\frac{1}{r}\frac{\partial u_r}{\partial\theta} + \frac{\partial u_\theta}{\partial r} - \frac{u_\theta}{r}\right) + 4u_r u_\theta\frac{\partial u_r}{\partial r}\right). \tag{54}$$

Using the analytical streamfunction (15) and parameterisation in the polar angle or radial distance, again allows the reduction of these equations to ODEs along streamlines.

In the viscometric wall boundary layer, we may use that $|u_\theta| \ll |u_r| \ll 1$ to see that $\nabla\cdot\mathbf{w} \sim -\dot\gamma/u_r^2$. The viscometric stress behaviour from (52) is given by

$$\begin{aligned} &\lambda + 2\mu\left(-\frac{\dot\gamma}{u_r^2}\right) + \kappa g_\lambda = \frac{1}{u_r^2}, \\ &\mu + \nu\left(-\frac{\dot\gamma}{u_r^2}\right) + \kappa g_\mu = 0, \\ &\nu + \kappa g_\nu = u_r^2. \end{aligned} \tag{55}$$

Consequently, for high shear rates $|\dot\gamma| \gg 1$, we have the viscometric behaviours

$$\begin{aligned} &\text{PTT:} \qquad \lambda \sim \left(\frac{\dot\gamma}{2\kappa}\right)^{\frac{2}{3}}\frac{2}{u_r^2}, \quad \mu \sim \left(\frac{\dot\gamma}{2\kappa}\right)^{\frac{1}{3}}, \quad \nu \sim u_r^2, \\ &\text{Giesekus:} \qquad \lambda \sim \left(\frac{2|\dot\gamma|}{\kappa}\right)^{\frac{1}{2}}\frac{a^{\frac{1}{2}}}{u_r^2}, \quad \mu \sim -a, \quad \nu \sim \left(\frac{2\kappa}{|\dot\gamma|}\right)^{\frac{1}{2}} a^{\frac{3}{2}}u_r^2, \end{aligned} \tag{56}$$

with a as given in (34). Keeping the largest terms only in (52) for this region, gives

$$\begin{aligned} &(\mathbf{u}\cdot\nabla)\lambda + 2\mu\left(-\frac{\dot\gamma}{u_r^2}\right) + \kappa\lambda^2 u_r^2 = 0, \\ &(\mathbf{u}\cdot\nabla)\mu + \nu\left(-\frac{\dot\gamma}{u_r^2}\right) + \kappa\lambda\mu u_r^2 = 0, \\ &(\mathbf{u}\cdot\nabla)\nu + \kappa\hat g_\nu = 0, \end{aligned} \tag{57}$$

where here

$$\hat g_\nu = \begin{cases} \lambda u_r^2(\nu - u_r^2), & \text{PTT}, \\ (\mu^2 - a^2)u_r^2, & \text{Giesekus}. \end{cases} \tag{58}$$

These constitute the wall boundary layer equations for the natural stress variables. The breakdown of this viscometric region occurs when the radial strain-rate dominates, which occurs from the first equation in (55) when $\dot e\lambda = O(\lambda^2 u_r^2)$ or $\dot e = O(\lambda u_r^2)$. Using (56) then gives the all important relationship between the radial and shear strain rates in (36) from which (37) follow.

For the behaviour in the stretching region, we note that (50) is an asymptotic solution to (20), when

$$\frac{\nu}{||\mathbf{u}||^2} \ll \mu \ll \lambda||\mathbf{u}||^2.$$

The natural stress equations (52) then reduce to

$$(\mathbf{u}\cdot\nabla)\lambda = 0, \qquad (\mathbf{u}\cdot\nabla)\mu = 0, \qquad (\mathbf{u}\cdot\nabla)\nu = 0, \tag{59}$$

so that the natural stresses are constant along streamlines (see also [80] and [79]) and hence functions of the streamfunction only. The expression (50) now provides the correction terms to the particular solution (21). We take their dependencies on the streamfunction in the power law forms

$$\lambda = C_1\left(\frac{\psi}{C_0}\right)^{n_1}, \qquad \mu = C_2\left(\frac{\psi}{C_0}\right)^{n_2}, \qquad \nu = C_3\left(\frac{\psi}{C_0}\right)^{n_3}, \tag{60}$$

which allows matching to their viscometric wall boundary layer behaviours. Each variable has an associated free constant, C_1, C_2, or C_3, which transmit the necessary stress behaviour form the upstream wall boundary layer to the the downstream free slip boundary layer. Equating the expressions (60) to their viscometric behaviours (56) at the boundary layer break down (37) determines the exponents as

$$n_2 = \begin{cases} \frac{\lambda_0-1}{\lambda_0+5}, \\ 0, \end{cases} \qquad n_3 = \begin{cases} \frac{2(1+2\lambda_0)}{\lambda_0+5}, & \text{PTT}, \\ \frac{\lambda_0+3}{4}, & \text{Giesekus}, \end{cases} \tag{61}$$

with n_1 as given earlier in (23) and gives order of magnitude estimates of

$$\lambda = \begin{cases} O(r^{-\frac{2(\lambda_0+1)(\lambda_0+2)}{\lambda_0+5}}), \\ O(r^{-\frac{(\lambda_0+3)(\lambda_0+1)}{4}}), \end{cases} \quad \mu = \begin{cases} O(r^{\frac{(\lambda_0+1)(\lambda_0-1)}{\lambda_0+5}}), \\ O(1), \end{cases} \quad \nu = \begin{cases} O(r^{\frac{2(\lambda_0+1)(1+2\lambda_0)}{\lambda_0+5}}), & \text{PTT}, \\ O(r^{\frac{(\lambda_0+3)(\lambda_0+1)}{4}}), & \text{Giesekus}. \end{cases} \tag{62}$$

Near the slip surface, the streamfunction behaviour (41) implies that $\nabla.\mathbf{w} = o(1)$ and the equations (52) simplify to

$$\begin{aligned} &(\mathbf{u}\cdot\nabla)\lambda + \kappa\lambda^2 u_r^2 = 0, \\ &(\mathbf{u}\cdot\nabla)\mu + \kappa\lambda\mu u_r^2 = 0, \\ &(\mathbf{u}\cdot\nabla)\nu + \kappa\hat{g}_\nu = 0, \end{aligned} \tag{63}$$

where again $\hat{g}_\nu$ is as given in (58). These equations have an exact solution, which we pursue elsewhere. For now it is sufficient to note for the λ variable, parameterising streamlines with radial distance, gives the solution

$$\lambda = \frac{C_1\left(\frac{\psi}{C_0}\right)^{n_1}}{1 - \frac{\kappa}{(\lambda_0+1)}C_\alpha C_0 C_1\left(\frac{\psi}{C_0}\right)^{n_1} r^{\lambda_0+1}}, \tag{64}$$

which matches with its value (60) from the stretching region. It is worth noting that this solution is consistent with (48), in the sense that the stretching relationship $T^p_{rr} = \lambda u_r^2$ still holds in the this region for these variables (although λ is no longer constant along streamlines). The estimate of the slip boundary layer thickness can be obtained from the first equation in (63), which gives the order of magnitude estimate

$$\lambda u_r^2 = O(\dot{e}). \tag{65}$$

Using the value of λ from the stretching region (60) with velocity and radial strain estimates in (41) and (42), recovers the estimate (46).

5. Numerical verification along the analytical streamlines

Here we numerically verify the analytical results of sections 3 and 4 for selected separation angles. This has the two-fold benefit of giving added confirmation of the accuracy of the analytical results as well as additional insights into their numerical behaviour.

The polymer constitutive equations in both polar form (27) and natural stress form (52) are integrated along the theoretical streamlines (15). They are parameterised with the polar angle and the system of ODEs are numerically solved as an initial-value-problem. We start sufficiently far upstream where the viscometric stresses are imposed. Since it is the ratio ψ/C_0 that is important, we take $C_0 = -1$ for normalisation. MATLAB solver ode15s is used over an interval of integration for θ taken as $[10^{-6},\ \alpha - 10^{-10}]$ with tolerances AbsTol = RelTol = 10^{-10}. The model parameter $\kappa = 0.1$ is used with a separation angle $\alpha = 7\pi/6$.

First in Figure 4, we illustrate selected streamlines of (15) that pass close to the contact point singularity. The streamlines are geometrically self-similar due to the separable stream function. Also shown are the boundary layer thickness estimates at the wall and free surface from (37) and (46). Of note is that the slip boundary layers are slightly thicker than those at the wall for both models, as well those for Giesekus being narrower than for PTT at both surfaces. This same relative behaviour in thickness holds for all separation angles of interest. As the separation angle increases, boundary layers at both surfaces get thinner. The angle $\theta \approx 2.27$ is also shown and represents the line along which each streamline attains its minimal radial distance from the contact point singularity at the die exit. Consequently this is also the point at which the radial velocity u_r vanishes.

Figure 5 collates the results for the polar stresses along the streamline $\psi = -10^{-6}$. Shown are the polymeric stress profiles for both models in addition to the dyadic velocity components $\mathbf{u}\mathbf{u}^T$ present in the stretching solution (21). Estimates of $\lambda(\psi)$ are found by dividing each stress component with its corresponding dyadic component. Figure 6 shows the natural stress variables along the same streamline. The corresponding plots along $\psi = -10^{-12}$ are given in Figures 7 and 8. The stretching solution (21) requires λ to be constant throughout the main θ interval, which is also rquired for the other natural stress variables in the more general solution noted in section 4. The results along $\psi = -10^{-6}$ are certainly not convincing of these behaviours, suggesting that the radial distances are still too large for the asymptotic results. The corresponding results along $\psi = -10^{-12}$ are more supportive of the required constant behaviours for the natural stresses. We may refer to earlier Figure 3(b) for minimum radial distance estimates for given separation angle and streamfunction value. For $\psi = -10^{-6}$, $r_{min} \approx 10^{-4}$, whilst for $\psi = -10^{-12}$, $r_{min} \approx 10^{-9}$. This highlights the small radial distances that are required to capture the asymptotics.

Figure 9 confirms the singular behaviour in the stretching solution (24) along the three lines $\theta = \pi/2$, $\pi/3$ and $2\pi/3$. Similarly, the behaviour of the NSF variables in (62) is confirmed for the stretching region and is demonstrated in figure 10. Noteworthy for both models, is the slower rate of convergence for the polar stresses to their theoretical asymptotics as the line into the singularity moves from inside the die $\theta = \pi/3$ to outside the die $\theta = 2\pi/3$. This is not as evident for the natural stresses, which are noted to converge faster compared to the polar components.

Finally, figures 11 and 12 present the behaviour from all three regions, namely the stretching region, wall and free surface boundary layers. The normal radial stress, T^p_{rr}, and the λ component of the natural stresses are plotted against radial distance. Figure 11 illustrates results along the $\psi = -10^{-6}$ streamline and figure 12 the $\psi = -10^{-12}$ streamline. We plot viscometric behaviour for the polar stress from (31), (32) and (33), and for the natural stress from (55) and (56). To represent the flow behaviour in the stretching behaviour domain, we plot the stretching solution (40) and constant natural stress behaviour from (60). Equations (47) and (63) are solved and plotted to represent the free-surface region. The vertical lines represent the wall and free-surface boundary layer demarcation point estimates from (37) and (46). The

theoretical behaviours provide excellent approximations on the smaller streamline $\psi = -10^{-12}$, but still provide reasonable accuracy for the $\psi = -10^{-6}$ streamline.

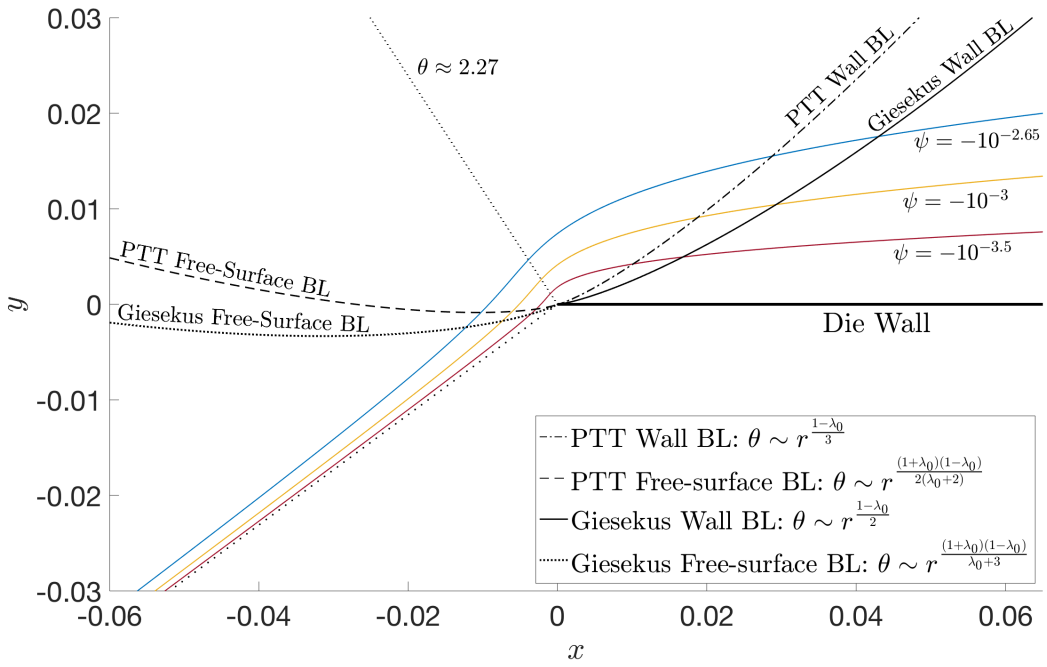

Figure 4: A plot of selected streamlines that pass near the singularity using (15) for $\alpha = 7\pi/6$ ($\lambda_0 \approx 0.3825$). Also shown are the boundary layer thickness estimates of both models. The line $\theta \approx 2.27$ represents the point of minimal radial distance, and where the radial velocity disappears, for each geometrically similar streamline.

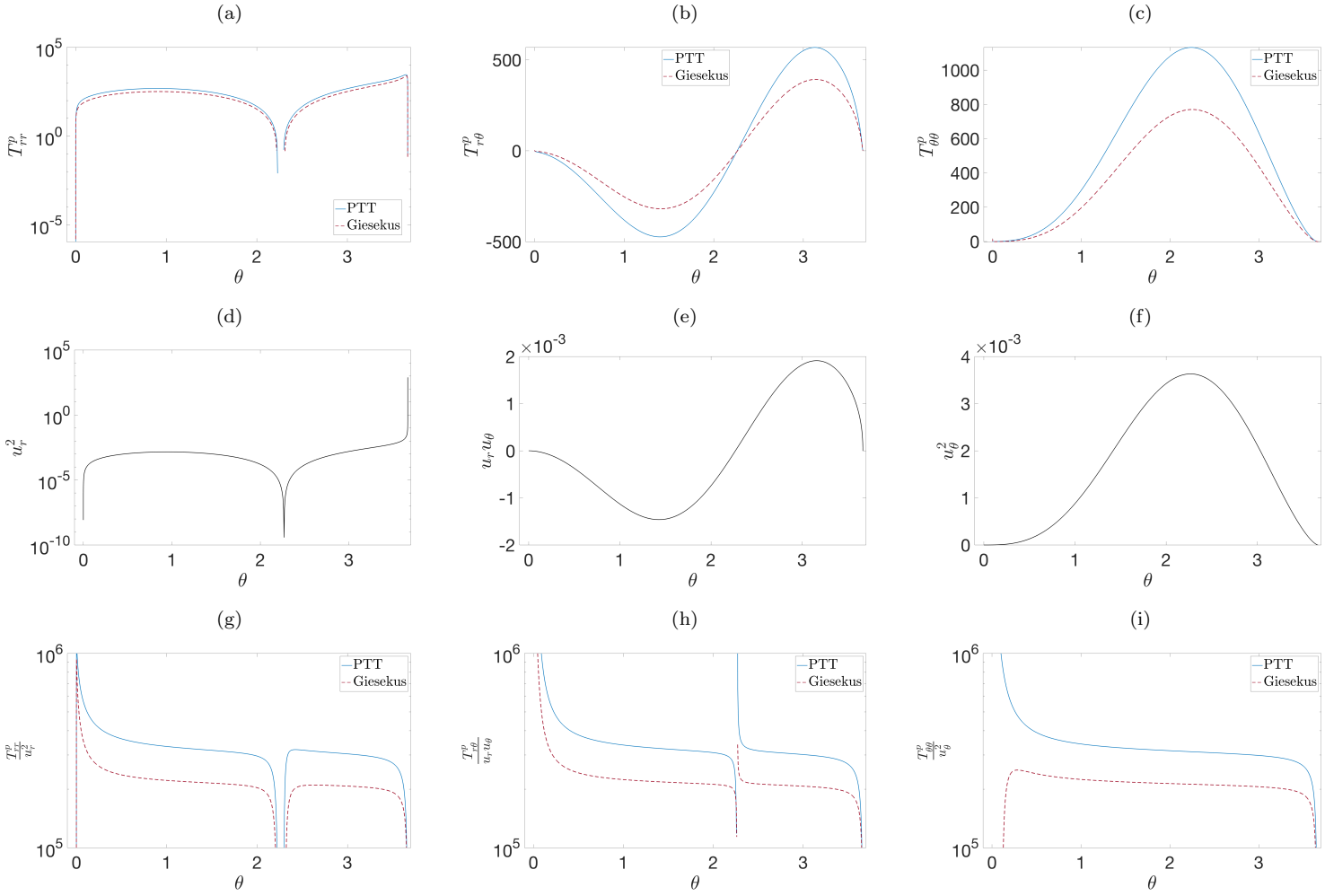

Figure 5: Polymeric stress components (a) T^p_{rr}, (b) $T^p_{r\theta}$ and (c) $T^p_{\theta\theta}$, dyadic velocity components (d) u_r^2, (e) $u_r u_\theta$, (f) u_θ^2 and (g)–(i) $\lambda(\psi)$ estimates found from the relevant ratio of stress to dyadic velocity component. The results shown are along streamline $\psi = -10^{-6}$, with separation angle $\alpha = \frac{7\pi}{6}$.

(a)

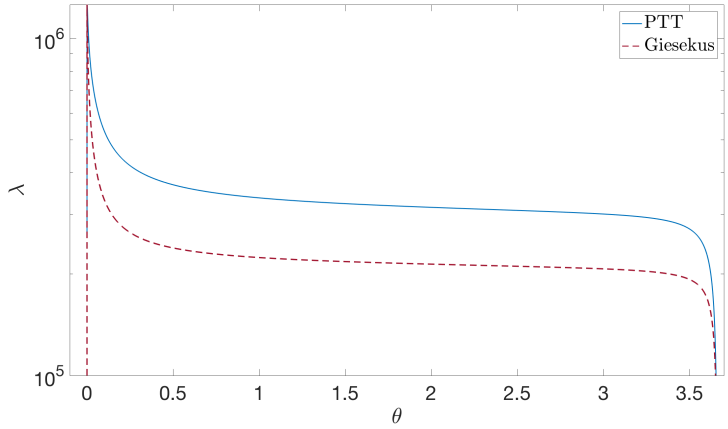

(b)

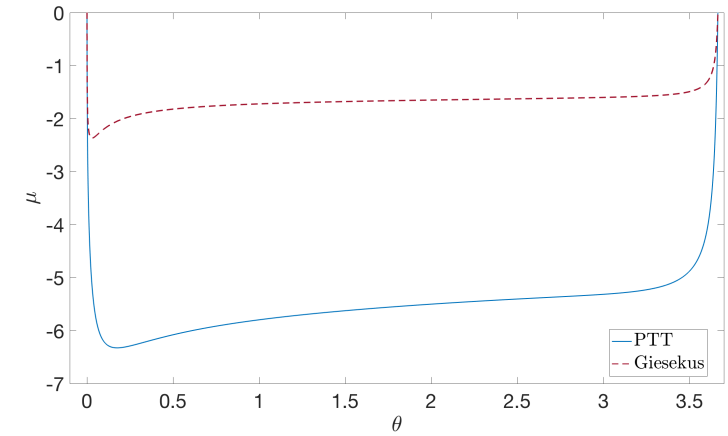

(c)

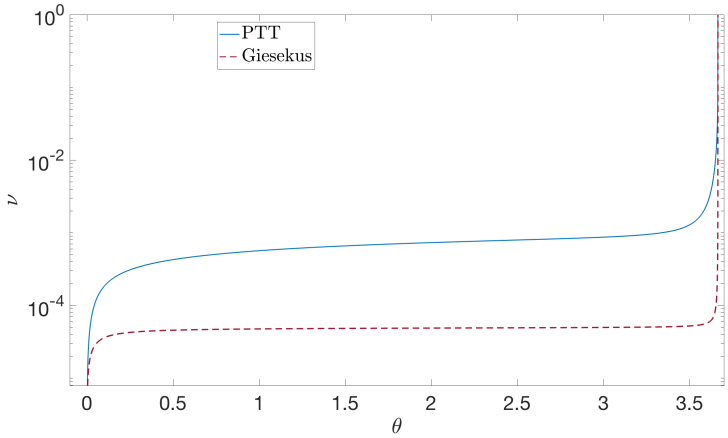

Figure 6: Natural stress components (a) λ, (b) μ and (c) ν plotted using (52) along the streamline $\psi = -10^{-6}$ with separation angle $\alpha = \frac{7\pi}{6}$.

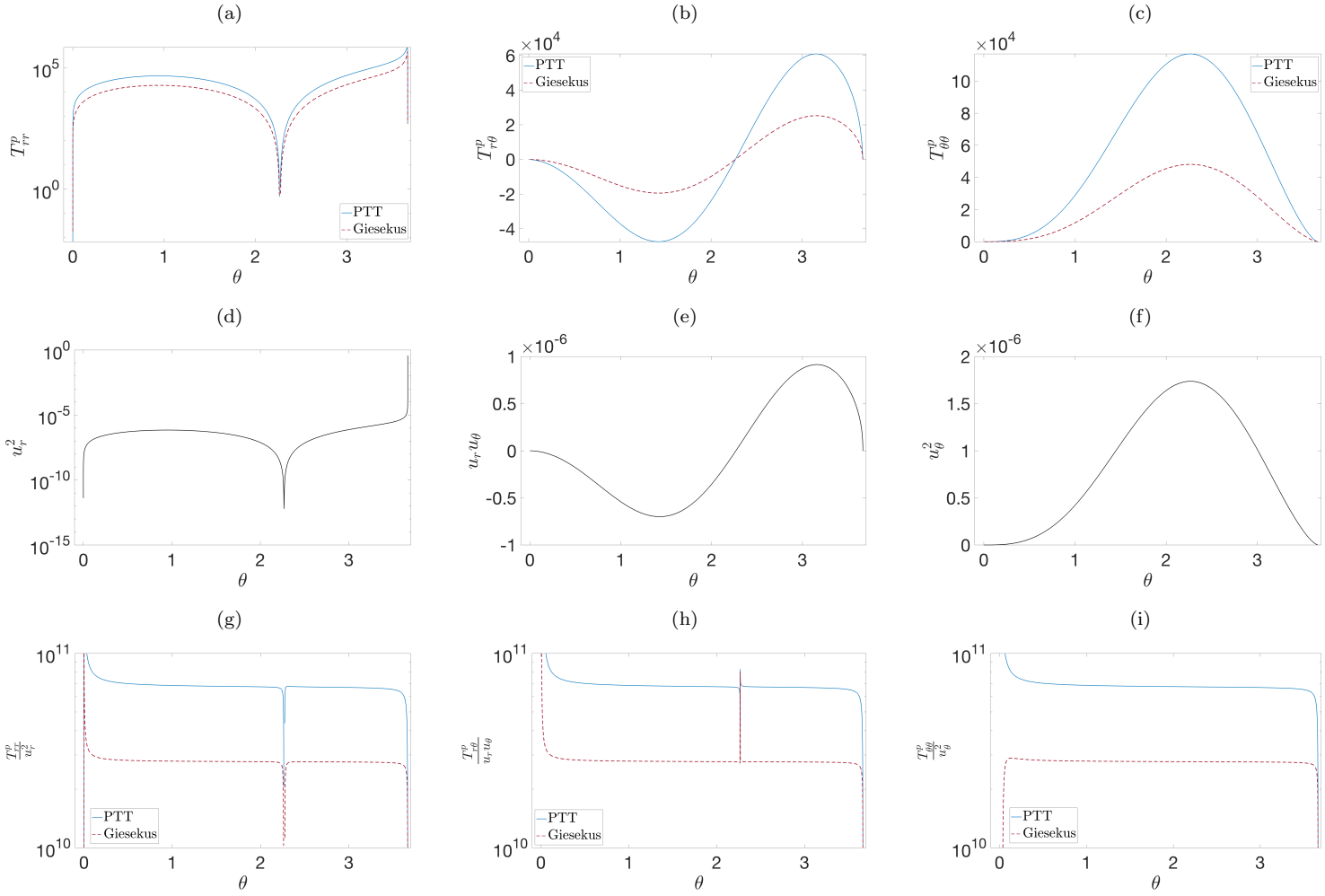

Figure 7: Polymeric stress components (a) T^p_{rr}, (b) $T^p_{r\theta}$ and (c) $T^p_{\theta\theta}$, dyadic velocity components (d) u_r^2, (e) $u_r u_\theta$, (f) u_θ^2 and (g)–(i) $\lambda(\psi)$ estimates found from the relevant ratio of stress to dyadic velocity component. The results shown are along streamline $\psi = -10^{-12}$, with separation angle $\alpha = \frac{7\pi}{6}$.

(a)

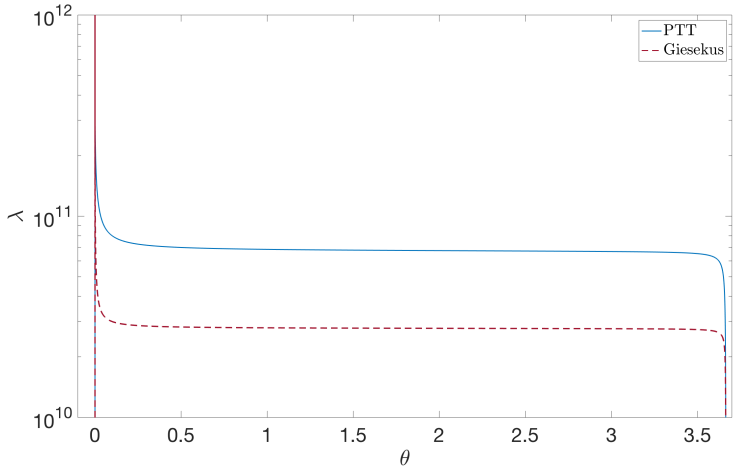

(b)

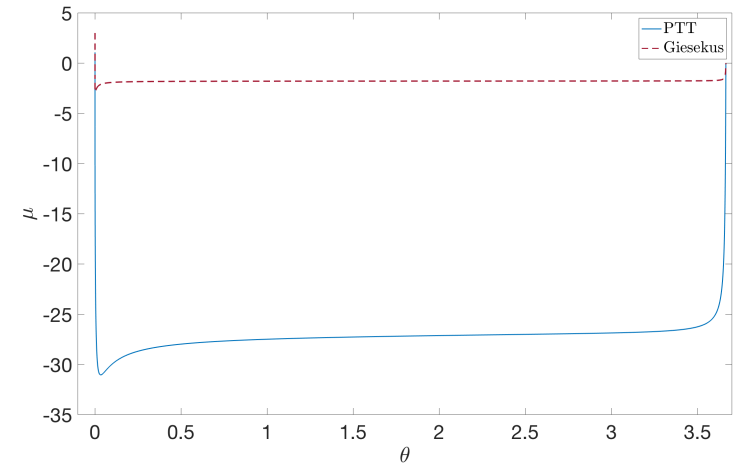

(c)

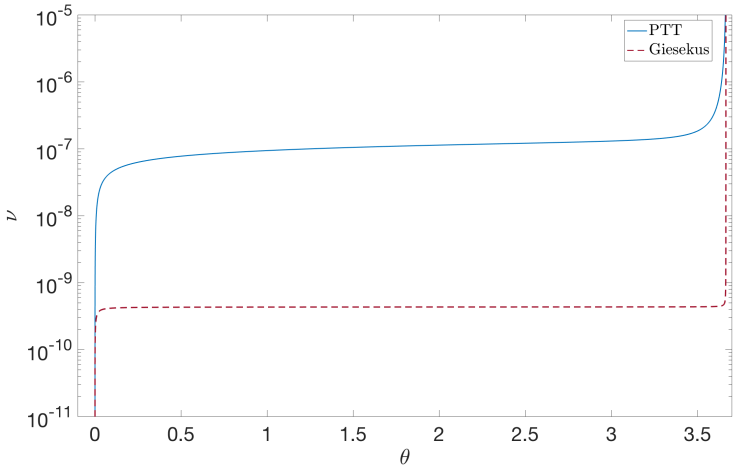

Figure 8: Natural stress components (a) λ, (b) μ and (c) ν plotted using (52) along the streamline $\psi = -10^{-12}$ with separation angle $\alpha = \frac{7\pi}{6}$.

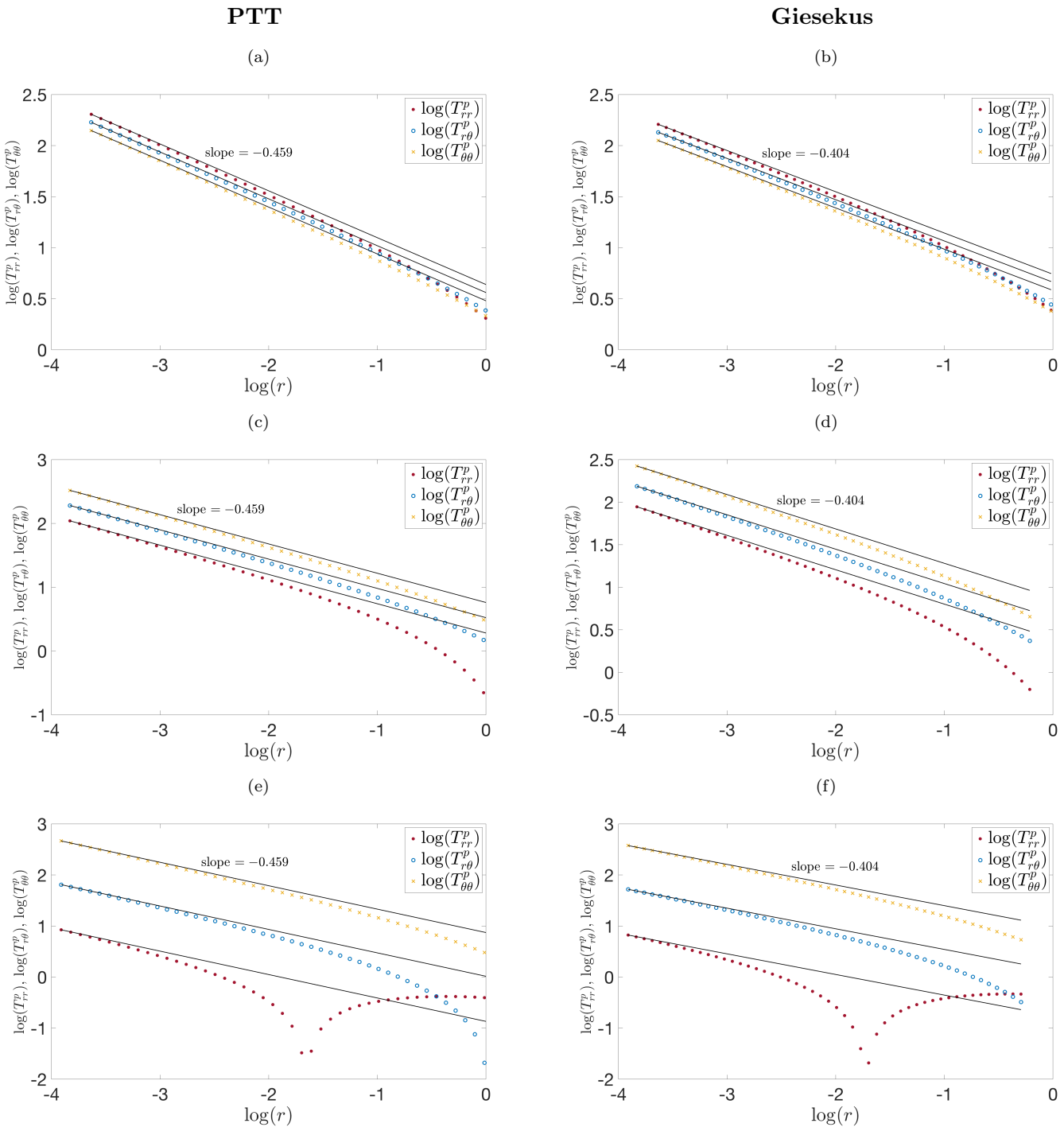

Figure 9: Verification of the stretching solution (40) along the lines (a)–(b) $\theta = \frac{\pi}{3}$, (c)–(d) $\theta = \frac{\pi}{2}$ and (e)–(f) $\theta = \frac{2\pi}{3}$ for $\alpha = \frac{7\pi}{6}$. The polymeric stress components are plotted using (27). The gradient slopes are the exponent values in (24). PTT: $\frac{-4(1-\lambda_0)}{\lambda_0+5} \approx -0.459$. Giesekus: $\frac{-(1-\lambda_0)(3-\lambda_0)}{4} \approx -0.404$.

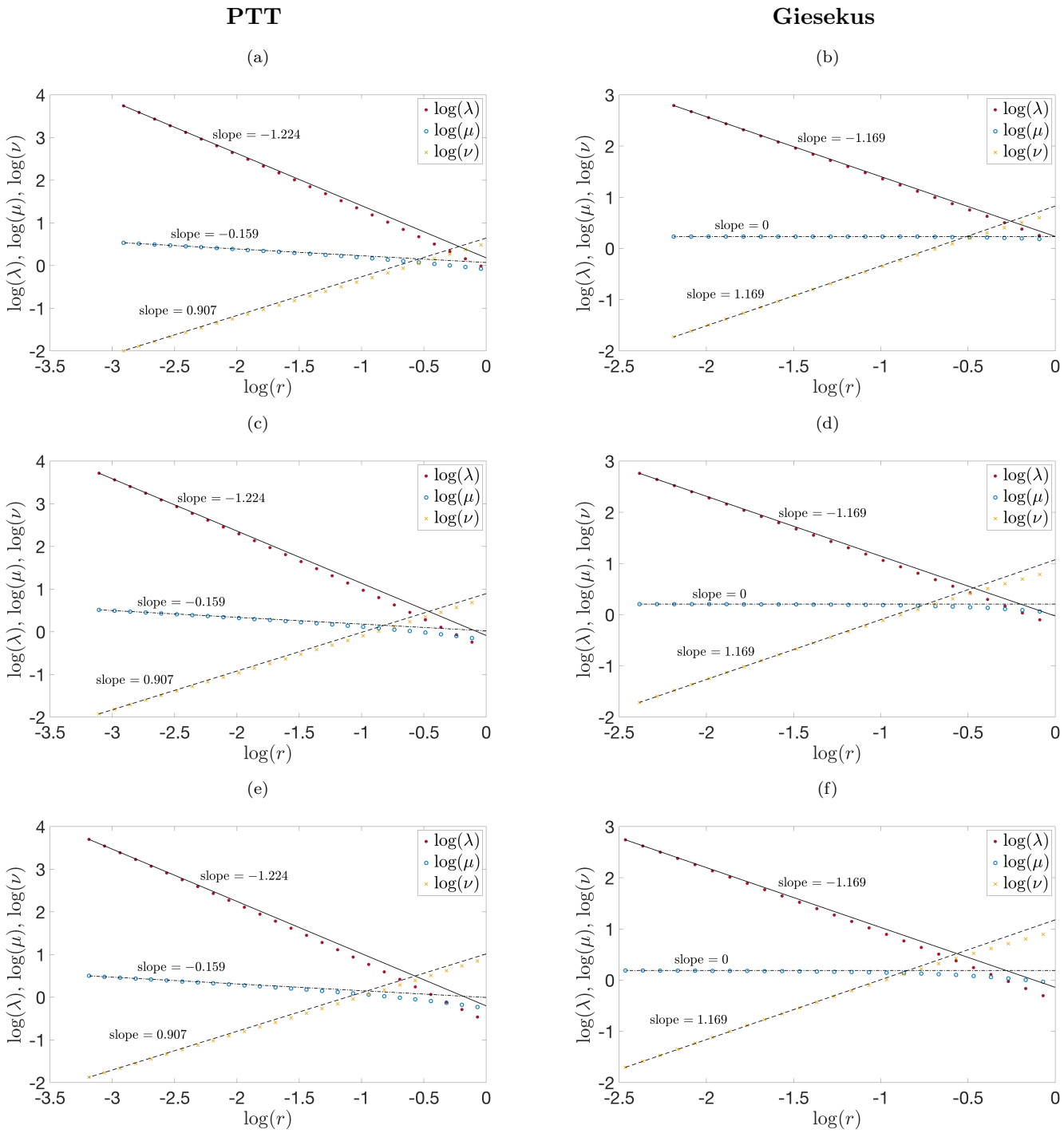

Figure 10: Verification of the stretching region NSF behaviour (62) along the lines (a)–(b) $\theta = \frac{\pi}{3}$, (c)–(d) $\theta = \frac{\pi}{2}$ and (e)–(f) $\theta = \frac{2\pi}{3}$ for $\alpha = \frac{7\pi}{6}$. The natural stress variables are plotted using (52). The gradient slopes are the exponent values in (62). PTT: $\frac{-2(\lambda_0+1)(\lambda_0+2)}{\lambda_0+5} \approx -1.224$, $\frac{-(1-\lambda_0)(\lambda_0+1)}{\lambda_0+5} \approx -0.159$ and $\frac{2(\lambda_0+1)(1+2\lambda_0)}{\lambda_0+5} \approx 0.907$. Giesekus: $\pm\frac{(\lambda_0+3)(\lambda_0+1)}{4} \approx \pm 1.169$.

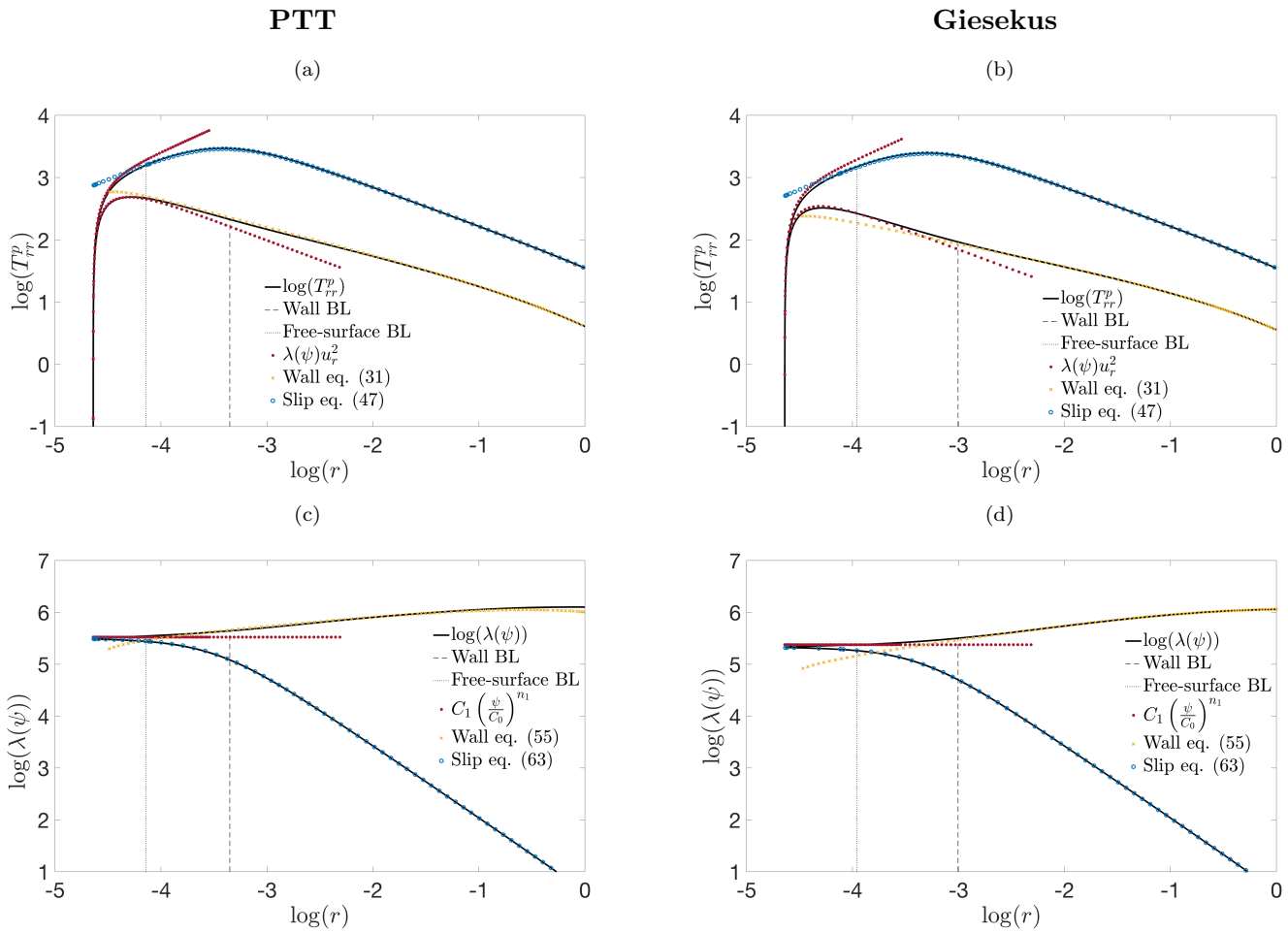

Figure 11: Behaviour of (a)–(b) $\log(T^p_{rr})$ and (c)–(d) $\log(\lambda)$ along the streamline $\psi = -10^{-6}$. Also plotted, for their corresponding constitutive model and choice of basis, are the viscometric behaviours (31) and (55); free-surface region behaviour from (47) and (63); stretching solution (40) and constant natural stress behaviour (60).

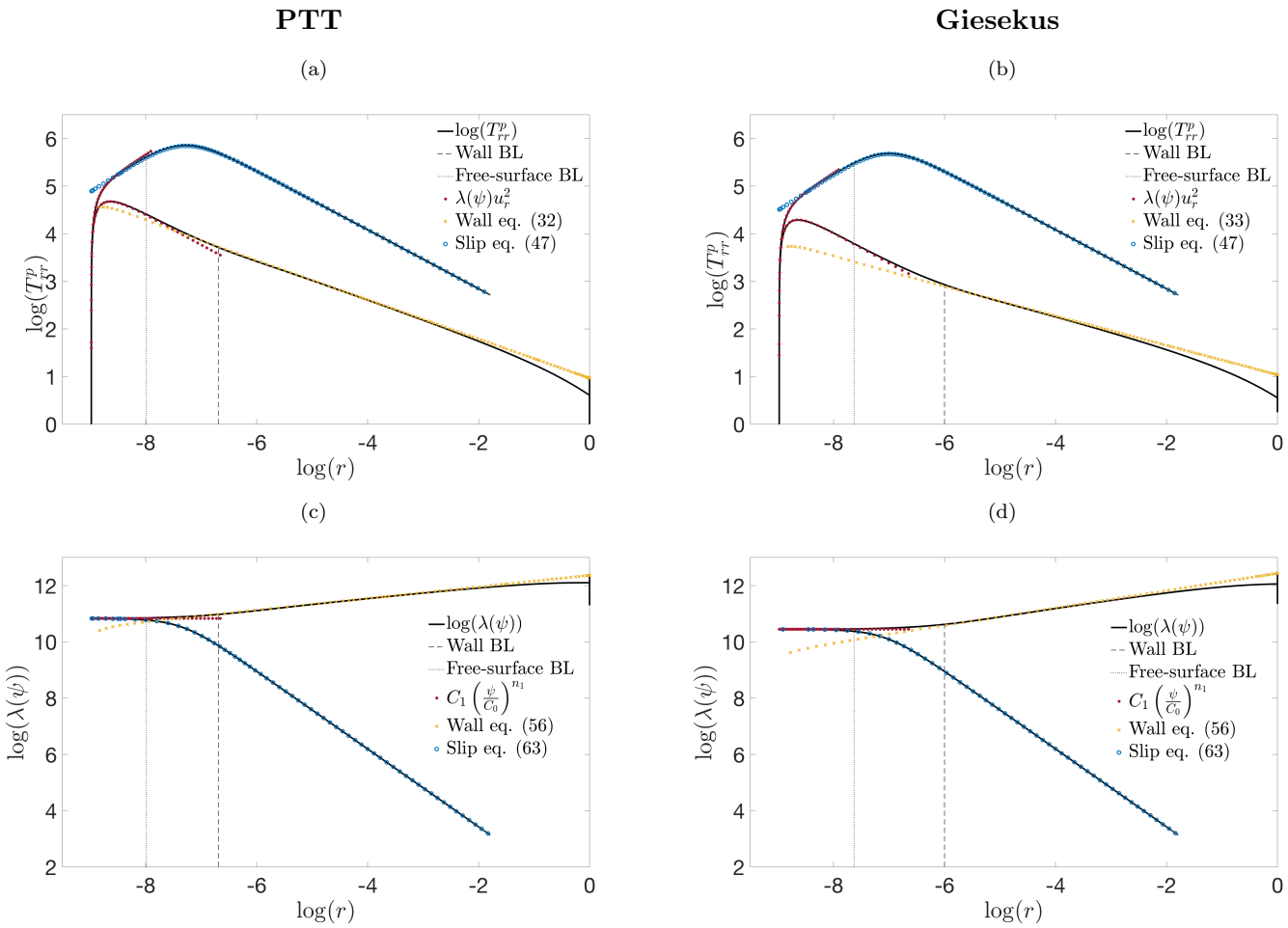

Figure 12: Behaviour of (a)–(b) $\log(T^p_{rr})$ and (c)–(d) $\log(\lambda)$ along the streamline $\psi = -10^{-12}$. Also plotted, for their corresponding constitutive model and choice of basis, are the viscometric behaviours (32), (33) and (56); free-surface region behaviour from (47) and (63); stretching solution (40) and constant natural stress behaviour (60).

6. Numerical simulation results

We now provide evidence that the theoretical behaviours for velocity and stress predicted in sections 3 and 4, are obtained by numerical simulations of the full extrudate swell problem.

A finite-volume numerical scheme for planar extrusion is used from the rheoTool toolbox [81] in OpenFOAM. The Eulerian free-surface solver of rheoInterFoam is implemented, which uses a volume of fluid (VOF) surface-capturing algorithm [82] to track the free-boundary. Details of the methodology are given in [58]. The geometry used for the planar extrusion simulations is shown in Figure 13, where here h is the die channel half-width we called h_0 in section 2. The narrow channel has length $35h$, with the wider channel slightly shorter at $25h$. The width of the wider channel is taken as $4h$, and also includes a $2.5h$ overlap above the die wall. These together ensure this region is large enough to have no real influence on the flow dynamics. We now summarise the numerical values set for the simulations:

1. The computation grid implemented is shown in Figure 14, with a summary of the main mesh statistics in Table 2. The mesh is highly refined near the die wall singularity, with the smallest mesh spacing being approximately 3×10^{-3}.

2. The scheme is transient, with a time-step taken of $\delta t = 10^{-7}s$. This ensures that the maximum Courant number $Co = \delta t \|\mathbf{U}\|/\delta x$ does not exceed 0.02, for stability. Here δx refers to the cell size in the direction of the velocity, and $\|\mathbf{U}\|$ the magnitude of the velocity through that cell. An endTime $= 120s$ terminates the simulation. The main solver tolerences used were: 10^{-10} in the stabilised preconditioned (bi)-conjugate gradient solver (PBICG) for the velocity and stress tensors, 10^{-8} in the generalised geometric-algebraic multi-grid solver (GAMG) for the pressure and 10^{-4} in smoothSolver for the fluid-air ratio (this being 0.5 for the free-surface).

3. The air/atmosphere is modelled as a Newtonian fluid with density ρ_{air} and viscosity η_{air}. The model parameters for the simulation are as follows:

Model Parameters

$\rho_{fluid} = 10^{-2}$,	$\rho_{air} = 10^{-4}$,	$\eta_s = 0.5$,	$\eta_p = 0.5$,	$\eta_{air} = 10^{-3}$,
$\kappa = 0.1$,	$\lambda_p = 1$,	$h = 1$,	$\bar{U} = \frac{1}{3}$,	$\dot{\gamma}_w = \frac{3\bar{U}}{h}$,	$\mathrm{Wi} = \lambda_p \dot{\gamma}_w$,

Table 1: Model parameters used for the numerical simulation.

which give the dimensionless parameter values $\beta = 0.5$, Wi $= 1$ and Re $= 3\rho_{fluid}\bar{U}/h = 10^{-2}$. The parameter $\bar{U}$ is defined as the average velocity at the inlet.

4. From the choice of high-resolution schemes available for the convective terms, the cubista scheme is implemented here. For the pressure-velocity coupling the SIMPLEC algorithm was chosen, with the Cartesian polymeric stresses being solved using a log-conformation representation. The natural stresses were also implemented in their direct form, without a log transformation.

The orientation of the geometry is opposite to that introduced in section 2. However, we still measure the polar angle located at the singularity from the die wall as shown in Figure 16.

Figure 15 shows the final extrudate swell situation with free-surface and selected streamlines. The separation angle is estimated as the angle of the tangent to the free-surface at the die wall edge or contact point. Its values for the two models are recorded in Table 3, along with the consequent Newtonian eigenvalue and the final extrudate swell ratio D_{extr}/h. We remark that swelling ratio is Weissenberg dependent, with larger values obtained as Weissenberg increases, as documented in [58]. The behaviours for the Cartesian velocities, pressure and polymeric stresses from the Cartesian log confirmation formulation are shown for PTT in Figure 17 and Giesekus in 19. For both models, results along all three angles show convincing convergence to the predicted theoretical values in (19) and (24). However, noticeable is that the three Cartesian stress components have different convergence rates, with T^p_{yy} in particular being slower than

Mesh Description	
Number of vertices	56310
Number of cell faces	110894
Number of cells	27580
Number of internal faces	54586
$\delta x/h = \delta y/h$ at $x = 0$, $y = h$	0.00316227766
$\delta y/h$ at $y = 0$, $-35h \leq x \leq 25h$	0.1982486592
$\delta x/h$ at $x = -35$, $0 \leq y \leq h$	1.697259608

Table 2: Summary statistics of the numerical grid.

the other two components. These results suggest that a finer grid resolution is needed before T^p_{yy} approaches its limiting value. Figure 18 and 20 show the results from the natural stress implementation. Better convergence of all three stress components to their theoretical values in (62) is now obtained at each angle. This highlights the advantages of using natural stresses over the Cartesian stresses. Importantly though, these simulation results are suggesting that the flow field is Newtonian dominated near the singularity and support convergence to the derived analytical results even at the grid spacing used.

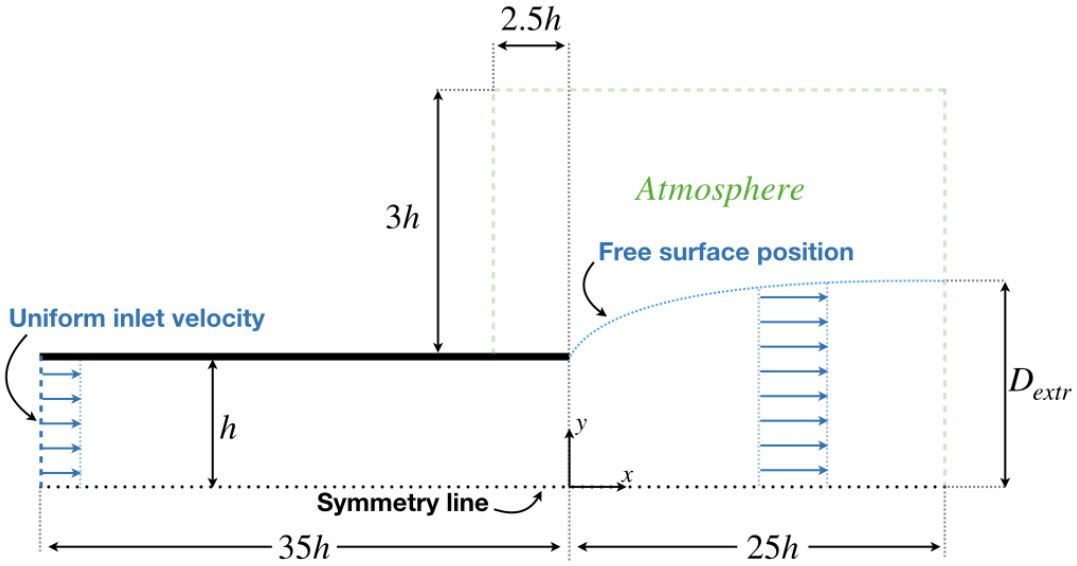

Figure 13: Geometry of the planar extrudate swell problem

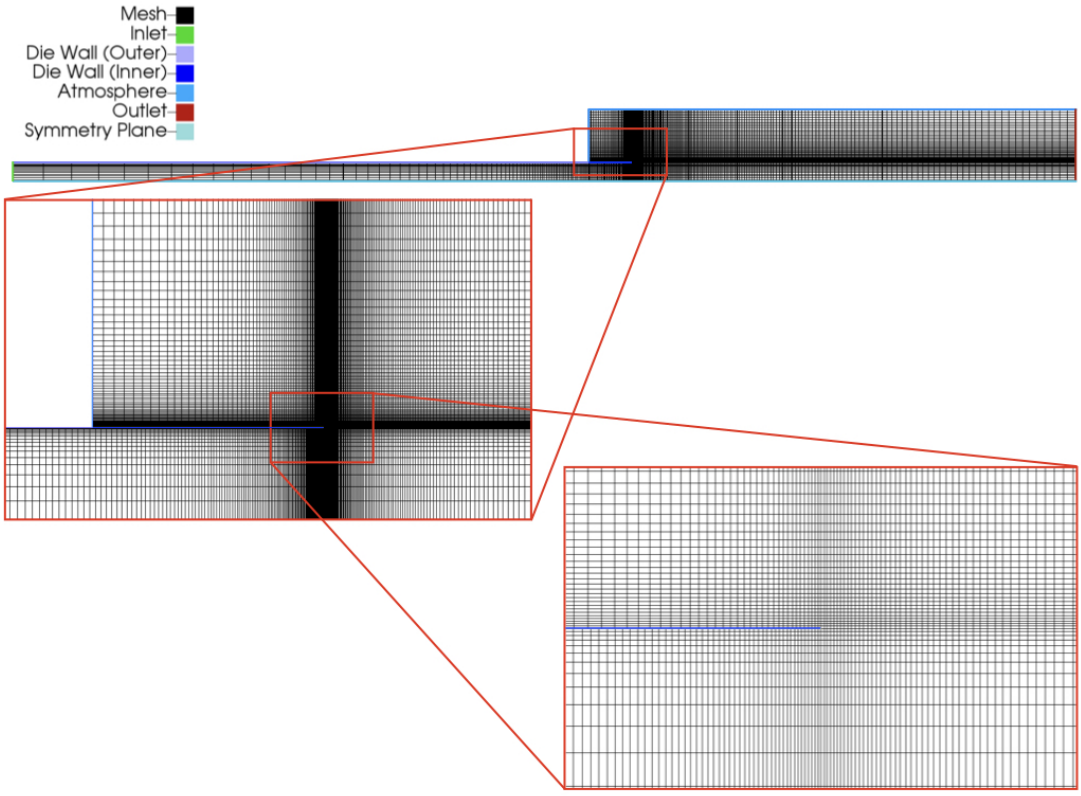

Figure 14: Computational grid

Numerical Estimations

	α		λ_0		D_{extr}/h	
	Cart	NSF	Cart	NSF	Cart	NSF
PTT	3.3580	3.3625	0.4401	0.4391	1.1854	1.1870
Giesekus	3.3516	3.3552	0.4417	0.4408	1.1808	1.1824

Table 3: Extrudate swell ratio, separation angle and corresponding lead eigenvalue.

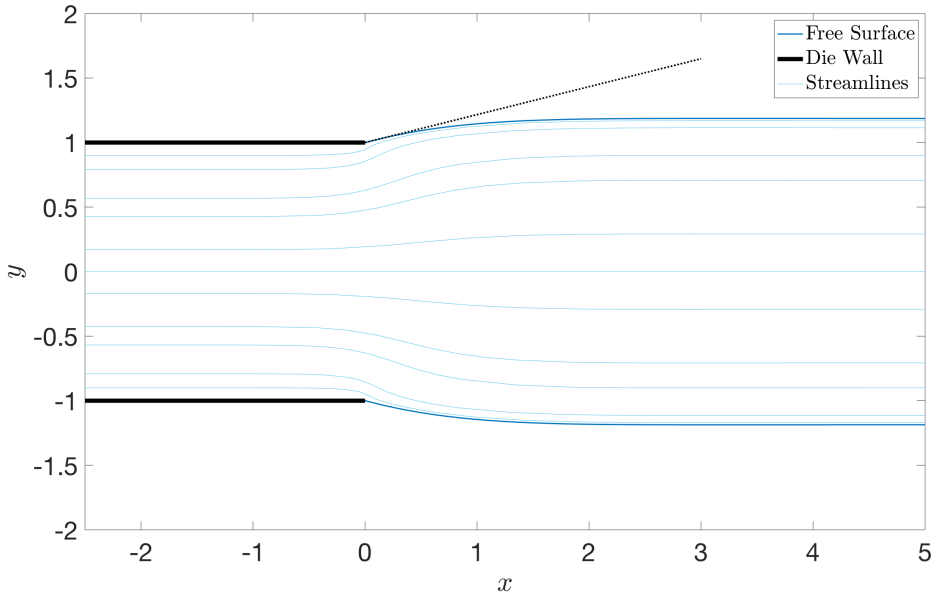

Figure 15: The final free surface position of the fluid, together with streamlines and separation angle.

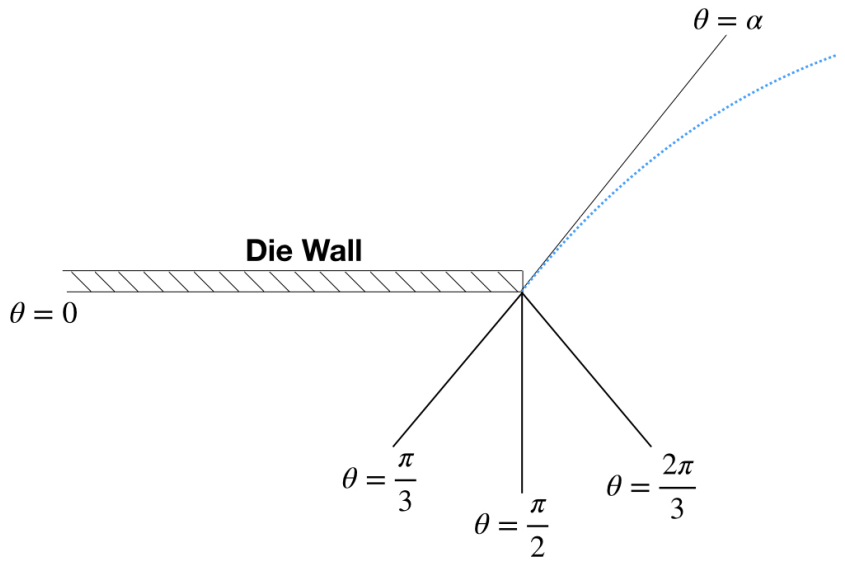

Figure 16: Local coordinate system at the edge of the upper die wall.

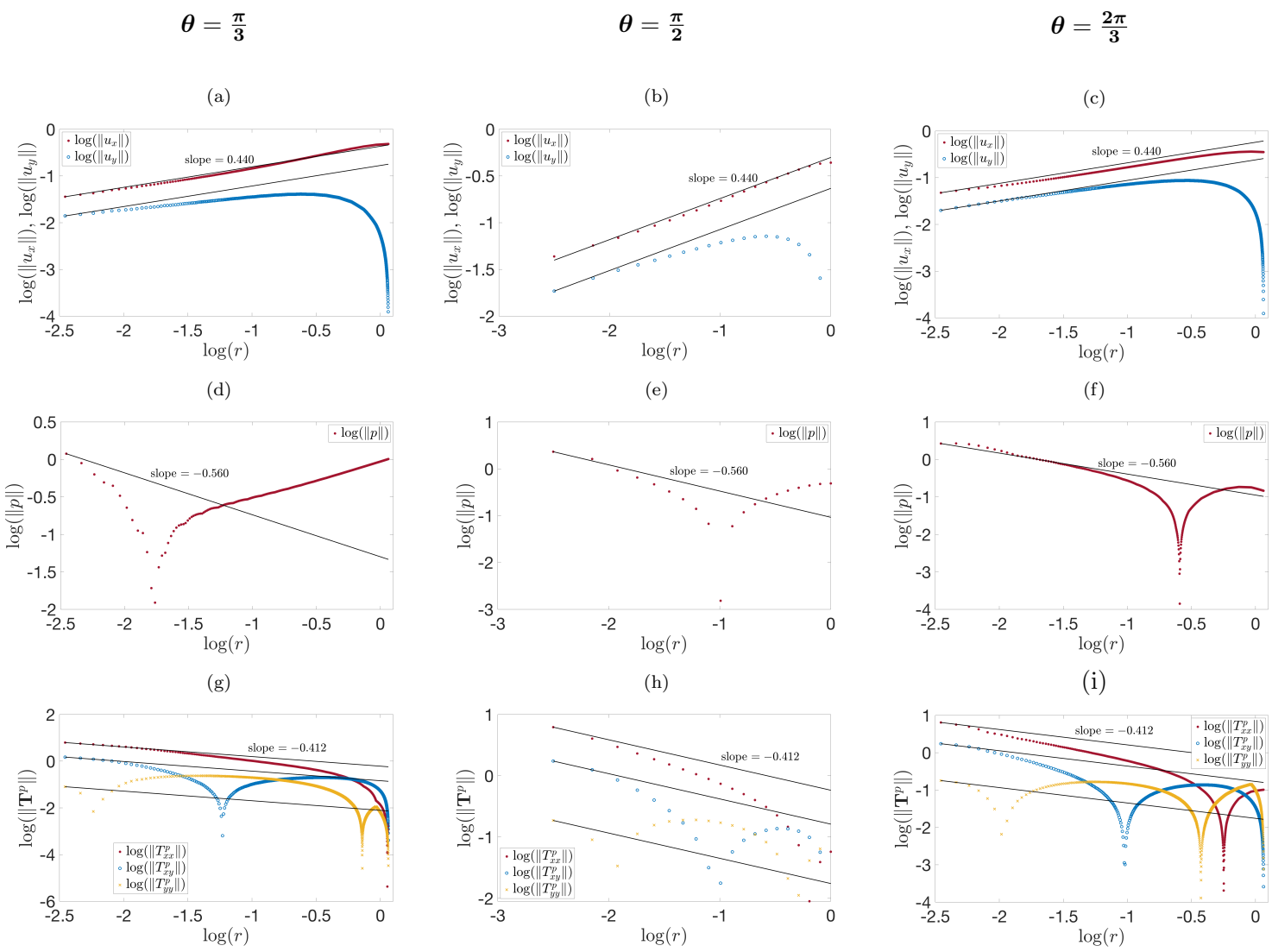

Figure 17: Limiting behaviour of (a)–(c) velocity components u_x and u_y, (d)–(f) pressure p and (g)–(i) polymeric stress components T^p_{11}, T^p_{12} and T^p_{22}. The left column presents the results along the line $\theta = \frac{\pi}{3}$, the middle column $\theta = \frac{\pi}{2}$ and the right column $\theta = \frac{2\pi}{3}$. The results plotted correspond to the linear PTT model solved in a Cartesian formulation with parameters, Wi $= 1$, $\kappa = 0.1$ and $\beta = 0.5$. Gradient lines: $\lambda_0 \approx 0.440$, $-(1-\lambda_0) \approx -0.560$, $\frac{-4(1-\lambda_0)}{\lambda_0+5} \approx -0.412$.

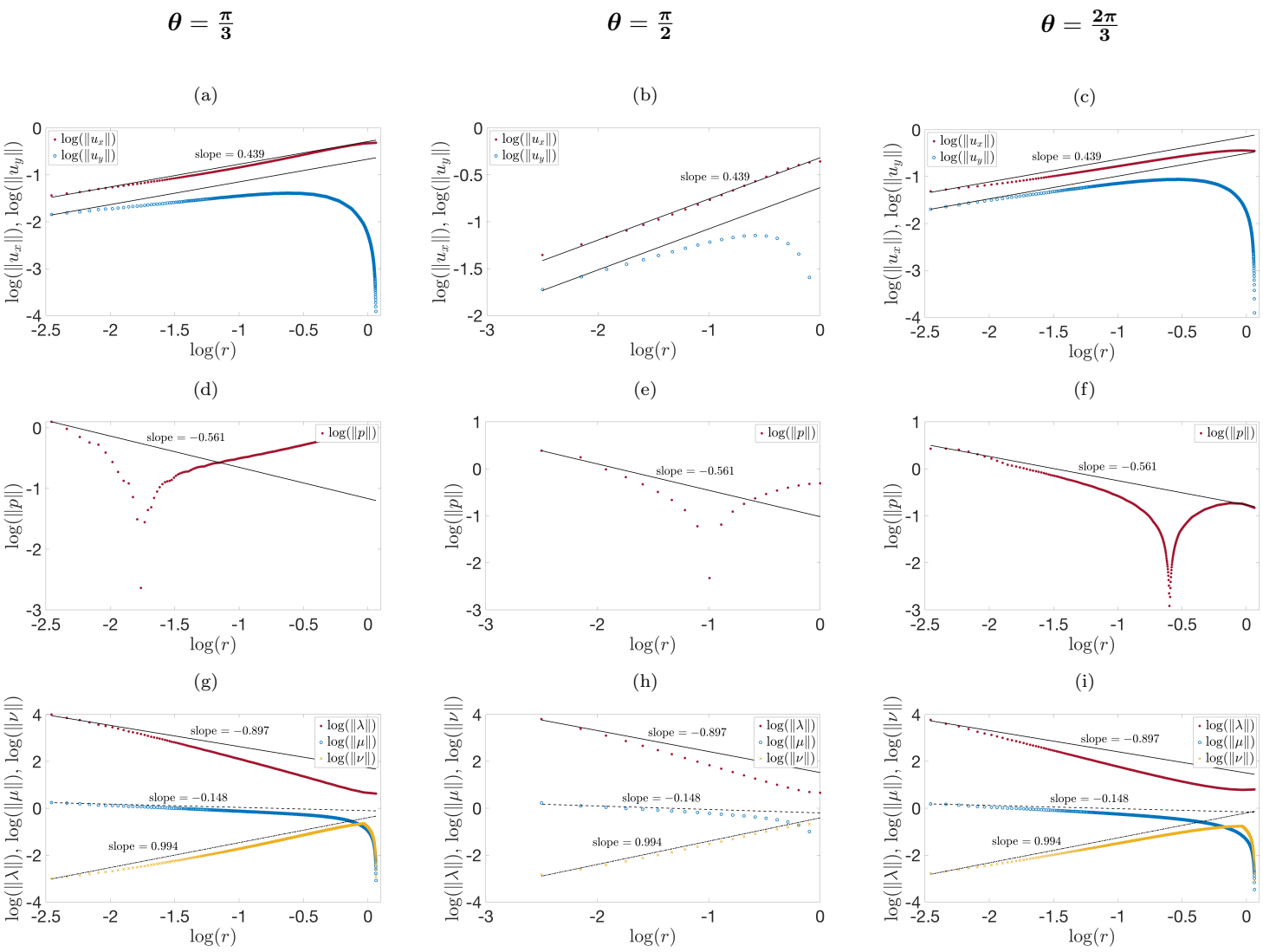

Figure 18: Limiting behaviour of (a)–(c) velocity components u_x and u_y, (d)–(f) pressure p and (g)–(i) natural stress components λ, μ and ν. The left column presents the results along the line $\theta = \frac{\pi}{3}$, the middle column $\theta = \frac{\pi}{2}$ and the right column $\theta = \frac{2\pi}{3}$. The results presented correspond to the linear PTT model solved in a natural stress formulation with parameters, Wi $= 1$, $\kappa = 0.1$ and $\beta = 0.5$. Gradient lines: $\lambda_0 \approx 0.439$, $-(1-\lambda_0) \approx -0.561$, $\frac{-2(\lambda_0+2)}{\lambda_0+5} \approx -0.897$, $\frac{-(1-\lambda_0)(\lambda_0+1)}{\lambda_0+5} \approx -0.148$, $\frac{2(\lambda_0+1)(1+2\lambda_0)}{\lambda_0+5} \approx 0.994$.

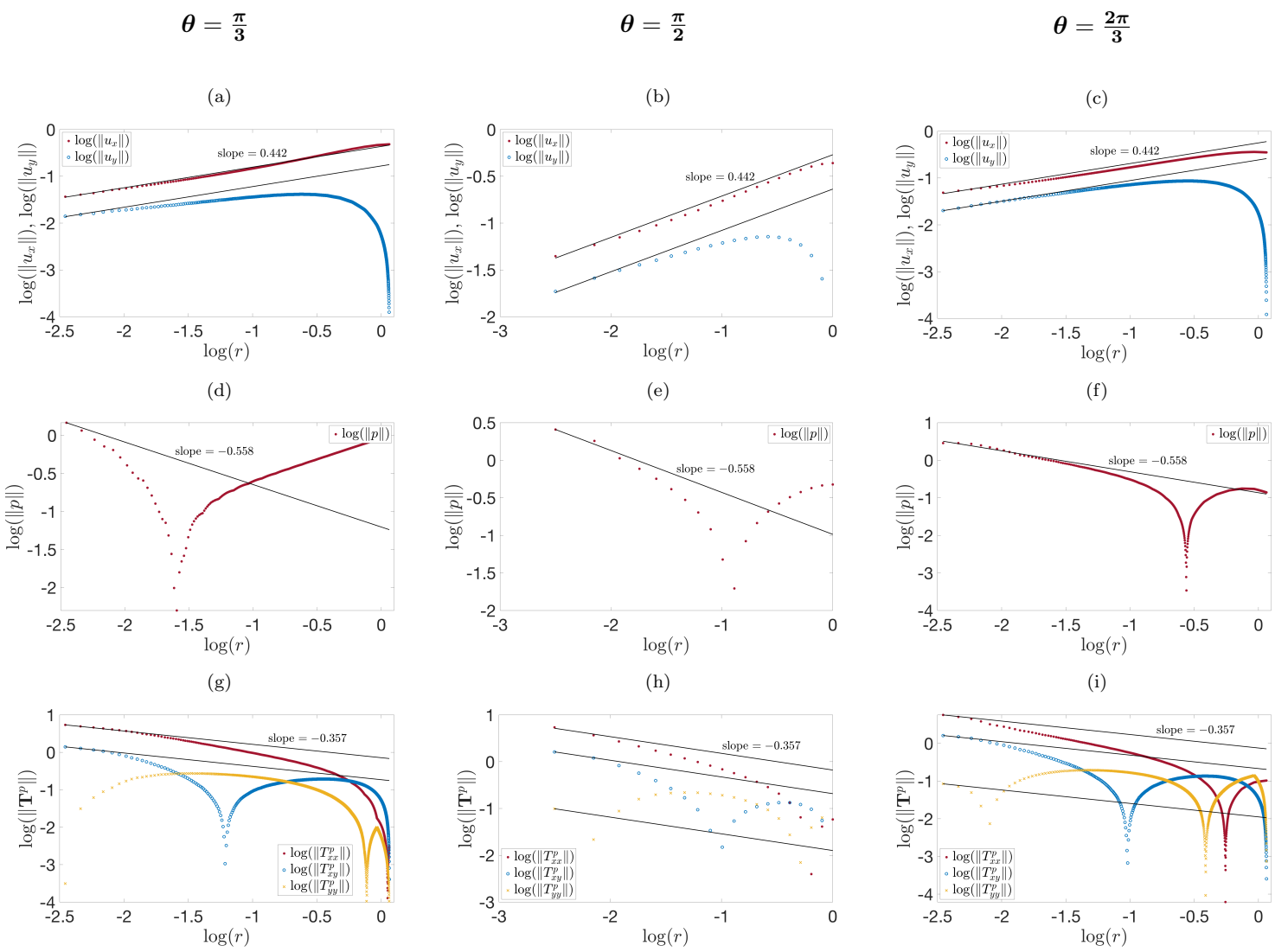

Figure 19: Limiting behaviour of (a)–(c) velocity components u_x and u_y, (d)–(f) pressure p and (g)–(i) polymeric stress components T^p_{11}, T^p_{12} and T^p_{22}. The left column presents the results along the line $\theta = \frac{\pi}{3}$, the middle column $\theta = \frac{\pi}{2}$ and the right column $\theta = \frac{2\pi}{3}$. The results plotted correspond to the Giesekus model solved in a Cartesian formulation with parameters, Wi $= 1$, $\kappa = 0.1$ and $\beta = 0.5$. Gradient lines: $\lambda_0 \approx 0.442$, $-(1-\lambda_0) \approx -0.558$, $\frac{-(1-\lambda_0)(3-\lambda_0)}{4} \approx -0.357$.

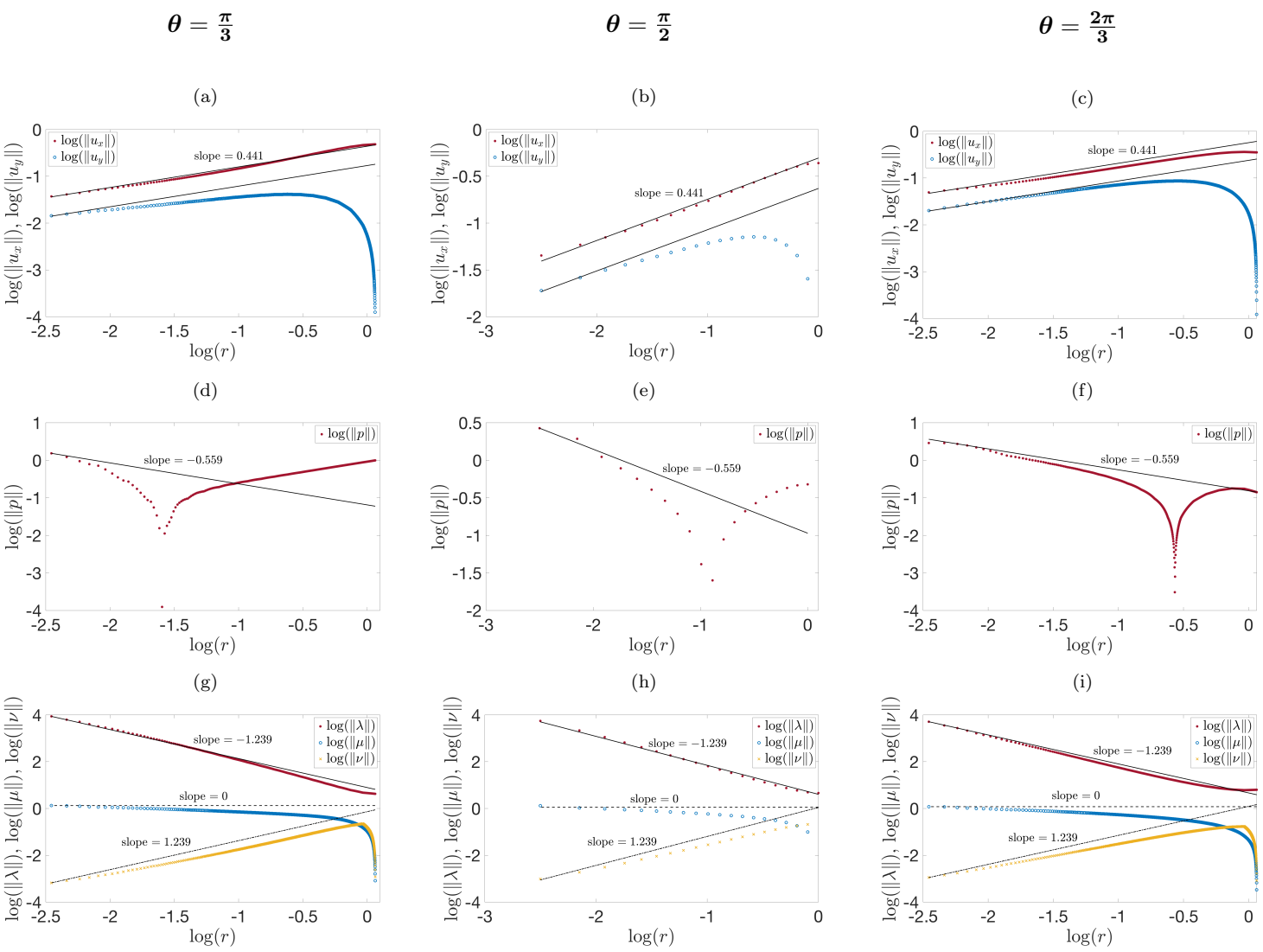

Figure 20: Limiting behaviour of (a)–(c) velocity components u_x and u_y, (d)–(f) pressure p and (g)–(i) natural stress components λ, μ and ν. The left column presents the results along the line $\theta = \frac{\pi}{3}$, the middle column $\theta = \frac{\pi}{2}$ and the right column $\theta = \frac{2\pi}{3}$. The results presented correspond to the Giesekus model solved in a natural stress formulation with parameters, Wi $= 1$, $\kappa = 0.1$ and $\beta = 0.5$. Gradient lines: $\lambda_0 \approx 0.441$, $-(1-\lambda_0) \approx -0.559$, $\pm\frac{(\lambda_0+3)(\lambda_0+1)}{4} \approx \pm 1.239$.

7. Discussion

An outstanding issue for viscoelastic fluids has been the nature of the singularity at the die edge in extrudate swell. This has been determined here for the PTT and Giesekus models, which can capture shear thinning behaviours often observed for real polymeric fluids. For both models, the asymptotic structure at the die edge singularity is similar, with boundary layers present at the die wall and free-surface, which are linked through a stretching region in which the polymer convects and deforms affinely. The flow field is locally Newtonian-like, since for both models the solvent stress dominates the polymer stress. Consequently the total extra-stress has the same singularity as the velocity gradients and controlled by the leading Newtonian eigenvalue as given in (19). The subdominance of the polymer stress (24) is a consequence of the influence of the shear-thinning quadratic stress terms that the constitutive equations of both models possess. Several comments are worth making:

1. Order of magnitude estimates only have been used to derive the results of the polymer stress singularity and boundary layer thicknesses. The resulting expressions have been verified through the numerical computations in section 5. Mathematically however, the polymer stresses should be asymptotically matched between the regions to demonstrate the correctness of the scalings for the stress variables.

2. The construction we present holds for all separation angles between 129^o and 270^o. At the smaller angle the singular velocity gradients are lost, whilst at the upper angle 270^o the form of the solution no longer holds (B_α in (15) is unbounded).

3. The asymptotic structure presented, is only valid when condition (13) holds. A necessary requirement then, is the presence of a solvent viscosity $0 < \beta \leq 1$ for the models and the results do not hold for the polymer melt situation of $\beta = 0$. This is due to the loss of the Newtonian velocity field. Implicit in our discussion is that $\kappa > 0$, so that the quadratic stress terms are present. In the case $\kappa = 0$, both models reduce to Oldroyd-B, for which condition (13) again does not hold. In this case, although β may be non-zero, the lack of the quadratic stress terms in the model means that the polymer stress now dominates the solvent stress, irrespective of the presence of the solvent viscosity. Thus the two isolated parameter cases $\beta = 0$ and $\kappa = 0$ remain to be addressed.

4. The results derived do not depend upon the size of the Weissenberg number, which has been conveniently set to unity. Its size does influence the spatial convergence rate of the stresses to their singular behvaiour, or equivalently the range of influence of the singularity. The full numerical simulation results in section 6, indicate that the numerical schemes do converge to the theoretical behaviours presented. Introducing these analytical solutions into numerical schemes at the singular point, is future work that will help stabilise codes and aid convergence, particularly for the problematic high Weissenberg numbers.

Acknowledgements

This work was supported by Sun Chemical Ltd and University of Bath through a 50:50 scholarship and FAPESP-SPRINT grant no. 2018/22242-0.

References

[1] J. R. Pearson, *Mechanics of Polymer Processing*. Springer Netherlands, 1985.

[2] R. G. Larson, "Instabilities in viscoelastic flows," *Rheologica Acta*, vol. 31, pp. 213–263, May 1992.

[3] M. M. Denn, "Extrusion instabilities and wall slip," *Annual Review of Fluid Mechanics*, vol. 33, no. 1, pp. 265–287, 2001.

[4] D. B. Harmon, "Drop sizes from low speed jets," *Journal of the Franklin Institute*, vol. 259, no. 6, pp. 519 – 522, 1955.

[5] S. Middleman and J. Gavis, "Expansion and contraction of capillary jets of Newtonian liquids," *The Physics of Fluids*, vol. 4, no. 3, pp. 355–359, 1961.

[6] S. L. Goren and S. Wronski, "The shape of low-speed capillary jets of Newtonian liquids," *Journal of Fluid Mechanics*, vol. 25, no. 1, p. 185–198, 1966.

[7] J. Batchelor, J. P. Berry, and F. Horsfall, "Die swell in elastic and viscous fluids," *Polymer*, vol. 14, no. 7, pp. 297 – 299, 1973.

[8] R. L. Gear, M. Keentok, J. F. Milthorpe, and R. I. Tanner, "The shape of low Reynolds number jets," *The Physics of Fluids*, vol. 26, no. 1, pp. 7–9, 1983.

[9] W. W. Graessley, S. D. Glasscock, and R. L. Crawley, "Die swell in molten polymers," *Transactions of the Society of Rheology*, vol. 14, no. 4, pp. 519–544, 1970.

[10] L. A. Utracki, Z. Bakerdjian, and M. R. Kamal, "A method for the measurement of the true die swell of polymer melts," *Journal of Applied Polymer Science*, vol. 19, no. 2, pp. 481–501, 1975.

[11] D. C. Huang and J. L. White, "Extrudate swell from slit and capillary dies: An experimental and theoretical study," *Polymer Engineering & Science*, vol. 19, no. 9, pp. 609–616, 1979.

[12] S. Richardson, "A 'stick-slip' problem related to the motion of a free jet at low Reynolds numbers," *Mathematical Proceedings of the Cambridge Philosophical Society*, vol. 67, no. 2, p. 477–489, 1970.

[13] R. I. Tanner and X. Huang, "Stress singularities in non-newtonian stick-slip and edge flows," *Journal of Non-Newtonian Fluid Mechanics*, vol. 50, no. 2, pp. 135 – 160, 1993.

[14] L. Sturges, "Die swell: The separation of the free surface," *Journal of Non-Newtonian Fluid Mechanics*, vol. 6, no. 2, pp. 155–159, 1979.

[15] M. Zidan, "Zur rheologie des spinnprozesses," *Rheologica Acta*, vol. 8, pp. 89–123, 03 1969.

[16] S. A. Trogdon and D. D. Joseph, "The stick-slip problem for a round jet," *Rheologica Acta*, vol. 19, pp. 404–420, Jul 1980.

[17] C. J. Coleman, "A note on the stick-slip and die-swell problems for a second-order fluid," *Journal of Non-Newtonian Fluid Mechanics*, vol. 3, no. 3, pp. 288 – 292, 1978.

[18] L. D. Sturges, "A theoretical study of extrudate swell," *Journal of Non-Newtonian Fluid Mechanics*, vol. 9, no. 3, pp. 357 – 378, 1981.

[19] S. Richardson, "The die swell phenomenon," *Rheologica Acta*, vol. 9, pp. 193–199, Apr 1970.

[20] J. Gavis and M. Modan, "Expansion and contraction of jets of Newtonian liquids in air: Effect of tube length," *The Physics of Fluids*, vol. 10, no. 3, pp. 487–497, 1967.

[21] D. D. Joseph, "Slow motion and viscometric motion; stability and bifurcation of the rest state of a simple fluid," *Archive for Rational Mechanics and Analysis*, vol. 56, pp. 99–157, Jun 1974.

[22] A. S. Lodge, *Elastic liquids: an introductory vector treatment of finite-strain polymer rheology.* Academic Press, 1964.

[23] A. B. Metzner, W. T. Houghton, R. A. Sailor, and J. L. White, "A method for the measurement of normal stresses in simple shearing flow," *Transactions of the Society of Rheology*, vol. 5, no. 1, pp. 133–147, 1961.

[24] J. C. Slattery and W. R. Schowalter, "Effect of surface tension in the measurement of the average normal stress at the exit of a capillary tube through an analysis of the capillary jet," *Journal of Applied Polymer Science*, vol. 8, no. 5, pp. 1941–1947, 1964.

[25] J. M. Davies, J. F. Hutton, and K. Walters, "Theory for normal stresses in slits and capillaries," *Journal of Physics D: Applied Physics*, vol. 6, no. 18, pp. 2259–2266, 1973.

[26] J. M. Davies, J. F. Hutton, and K. Walters, "A critical re-appraisal of the jet-thrust technique for normal stresses, with particular reference to axial velocity and stress rearrangement at the exit plane," *Journal of Non-Newtonian Fluid Mechanics*, vol. 3, no. 2, pp. 141 – 160, 1977.

[27] D. V. Boger and M. M. Denn, "Capillary and slit methods of normal stress measurements," *Journal of Non-Newtonian Fluid Mechanics*, vol. 6, no. 3, pp. 163 – 185, 1980.

[28] R. R. Huilgol, "Some qualitative and quantitative features of die swell," *Polymer Engineering & Science*, vol. 18, no. 8, pp. 643–648, 1978.

[29] R. I. Tanner, "Die-swell reconsidered: some numerical solutions using a finite element program," *Appl. Polym. Symp.*, no. 20, pp. 201–208, 1973.

[30] R. E. Nickell, R. I. Tanner, and B. Caswell, "The solution of viscous incompressible jet and free-surface flows using finite-element methods," *Journal of Fluid Mechanics*, vol. 65, no. 1, p. 189–206, 1974.

[31] K. R. Reddy and R. I. Tanner, "Finite element solution of viscous jet flows with surface tension," *Computers and Fluids*, vol. 6, no. 2, pp. 83–91, 1978.

[32] M. J. Crochet and R. Keunings, "Die swell of a Maxwell fluid: numerical prediction," *Journal of Non-Newtonian Fluid Mechanics*, vol. 7, no. 2-3, pp. 199–212, 1980.

[33] P. Chang, T. W. Patten, and B. A. Finlayson, "Collocation and galerkin finite element methods for viscoelastic fluid flow-II. die swell problems with a free surface," *Computers and Fluids*, vol. 7, no. 4, pp. 285–293, 1979.

[34] B. J. Omodei, "Computer solutions of a plane Newtonian jet with surface tension," *Computers and Fluids*, vol. 7, no. 2, pp. 79–96, 1979.

[35] B. J. Omodei, "On the die-swell of an axisymmetric Newtonian jet," *Computers and Fluids*, vol. 8, no. 3, pp. 275–289, 1980.

[36] M. J. Crochet and R. Keunings, "Finite element analysis of die swell of a highly elastic fluid," *Journal of Non-Newtonian Fluid Mechanics*, vol. 10, no. 3, pp. 339 – 356, 1982.

[37] M. B. Bush, J. F. Milthorpe, and R. I. Tanner, "Finite element and boundary element methods for extrusion computations," *Journal of Non-Newtonian Fluid Mechanics*, vol. 16, no. 1, pp. 37 – 51, 1984.

[38] J. Clermont and M. Normandin, "Numerical simulation of extrudate swell for Oldroyd-B fluids using the stream-tube analysis and a streamline approximation," *Journal of Non-Newtonian Fluid Mechanics*, vol. 50, no. 2, pp. 193 – 215, 1993.

[39] S. Tanoue, T. Kajiwara, Y. Iemoto, and K. Funatsu, "High Weissenberg number simulation of an annular extrudate swell using the differential type constitutive equation," *Polymer Engineering & Science*, vol. 38, no. 3, pp. 409–419, 1998.

[40] G. Karapetsas and J. Tsamopoulos, "Steady extrusion of viscoelastic materials from an annular die," *Journal of Non-Newtonian Fluid Mechanics*, vol. 154, no. 2, pp. 136 – 152, 2008.

[41] M. Normandin, J. Clermont, J. Guillet, and C. Raveyre, "Three-dimensional extrudate swell experimental and numerical study of a polyethylene melt obeying a memory-integral equation," *Journal of Non-Newtonian Fluid Mechanics*, vol. 87, no. 1, pp. 1 – 25, 1999.

[42] G. Russo and T. N. Phillips, "Spectral element predictions of die-swell for Oldroyd-B fluids," *Computers & Fluids*, vol. 43, no. 1, pp. 107 – 118, 2011. Symposium on High Accuracy Flow Simulations. Special Issue Dedicated to Prof. Michel Deville.

[43] G. Russo and T. N. Phillips, "Numerical prediction of extrudate swell of branched polymer melts," *Rheologica Acta*, vol. 49, no. 6, pp. 657–676, 2010.

[44] V. Ganvir, A. Lele, R. Thaokar, and B. P. Gautham, "Prediction of extrudate swell in polymer melt extrusion using an Arbitrary Lagrangian Eulerian (ALE) based finite element method," *Journal of Non-Newtonian Fluid Mechanics*, vol. 156, no. 1, pp. 21 – 28, 2009.

[45] Y. Cao, X. Ren, X. Guo, M. Wang, Q. Wang, X. Xu, and X. Yang, "A new method to simulate free surface flows for viscoelastic fluid," *Advances in Materials Science and Engineering*, vol. 2015, pp. 1–10, 2015.

[46] J. Fang, R. G. Owens, T. L., and A. Parriaux, "A numerical study of the SPH method for simulating transient viscoelastic free surface flows," *Journal of Non-Newtonian Fluid Mechanics*, vol. 139, no. 1, pp. 68 – 84, 2006.

[47] A. Rafiee, M. T. Manzari, and M. Hosseini, "An incompressible SPH method for simulation of unsteady viscoelastic free-surface flows," *International Journal of Non-Linear Mechanics*, vol. 42, no. 10, pp. 1210 – 1223, 2007.

[48] X. Xu, J. Ouyang, T. Jiang, and Q. Li, "Numerical simulation of 3D-unsteady viscoelastic free surface flows by improved smoothed particle hydrodynamics method," *Journal of Non-Newtonian Fluid Mechanics*, vol. 177-178, pp. 109 – 120, 2012.

[49] M. F. Tomé, B. Duffy, and S. McKee, "A numerical technique for solving unsteady non-Newtonian free surface flows," *Journal of Non-Newtonian Fluid Mechanics*, vol. 62, no. 1, pp. 9 – 34, 1996.

[50] M. F. Tomé, A. C. Filho, J. A. Cuminato, N. Mangiavacchi, and S. Mckee, "GENSMAC3D: a numerical method for solving unsteady three-dimensional free surface flows," *International Journal for Numerical Methods in Fluids*, vol. 37, no. 7, pp. 747–796, 2001.

[51] M. F. Tomé, L. Grossi, A. Castelo, J. A. Cuminato, N. Mangiavacchi, V. G. Ferreira, F. S. de Sousa, and S. McKee, "A numerical method for solving three-dimensional generalized Newtonian free surface flows," *Journal of Non-Newtonian Fluid Mechanics*, vol. 123, no. 2, pp. 85 – 103, 2004.

[52] M. F. Tomé, A. Castelo, V. G. Ferreira, and S. McKee, "A finite difference technique for solving the Oldroyd-B model for 3D-unsteady free surface flows," *Journal of Non-Newtonian Fluid Mechanics*, vol. 154, no. 2, pp. 179 – 206, 2008.

[53] M. F. Tomé, G. S. Paulo, F. T. Pinho, and M. A. Alves, "Numerical solution of the PTT constitutive equation for unsteady three-dimensional free surface flows," *Journal of Non-Newtonian Fluid Mechanics*, vol. 165, no. 5, pp. 247 – 262, 2010.

[54] G. Mompean, L. Thais, M. F. Tomé, and A. Castelo, "Numerical prediction of three-dimensional time-dependent viscoelastic extrudate swell using differential and algebraic models," *Computers & Fluids*, vol. 44, no. 1, pp. 68 – 78, 2011.

[55] R. A. Figueiredo, C. M. Oishi, J. A. Cuminato, and M. A. Alves, "Three-dimensional transient complex free surface flows: Numerical simulation of XPP fluid," *Journal Of Non-Newtonian Fluid Mechanics*, vol. 195, pp. 88–98, 2013.

[56] M. F. Tomé, J. Bertoco, C. M. Oishi, M. S. B. Araujo, D. Cruz, F. T. Pinho, and M. Vynnycky, "A finite difference technique for solving a time strain separable K-BKZ constitutive equation for two-dimensional moving free surface flows," *Journal of Computational Physics*, vol. 311, pp. 114–141, 2016.

[57] J. L. Favero, A. R. Secchi, N. S. M. Cardozo, and H. Jasak, "Viscoelastic fluid analysis in internal and in free surface flows using the software OpenFOAM," *Computers and Chemical Engineering*, vol. 34, no. 12, pp. 1984–1993, 2010.

[58] R. Comminal, F. Pimenta, J. H. Hattel, M. A. Alves, and J. Spangenberg, "Numerical simulation of the planar extrudate swell of pseudoplastic and viscoelastic fluids with the streamfunction and the VOF methods," *Journal of Non-Newtonian Fluid Mechanics*, vol. 252, no. C, pp. 1–18, 2018.

[59] J. P. Berry and J. Batchelor, "Application of the momentum balance theory of die-swell to polymer melts," *Research Report*, vol. 184, 1970.

[60] S. Richardson, "A 'stick-slip' problem related to the motion of a free jet at low Reynolds numbers," *Mathematical Proceedings of the Cambridge Philosophical Society*, vol. 67, no. 2, pp. 477–489, 1970.

[61] P. André and J. Clermont, "Numerical simulation of the die swell problem of a Newtonian fluid by using the concept of stream function and a local analysis of the singularity at the corner," *Journal of Non-Newtonian Fluid Mechanics*, vol. 23, pp. 335 – 354, 1987.

[62] R. I. Tanner, "A theory of die-swell revisited," *Journal of Non-Newtonian Fluid Mechanics*, vol. 129, no. 2, pp. 85 – 87, 2005.

[63] N. Phan-Thien and R. I. Tanner, "A new constitutive equation derived from network theory," *Journal of Non-Newtonian Fluid Mechanics*, vol. 2, no. 4, pp. 353–365, 1977.

[64] N. Phan-Thien, "A nonlinear network viscoelastic model," *Journal of Rheology*, vol. 22, no. 3, pp. 259–283, 1978.

[65] H. Giesekus, "A simple constitutive equation for polymer fluids based on the concept of deformation-dependent tensorial mobility," *Journal of Non-Newtonian Fluid Mechanics*, vol. 11, no. 1, pp. 69–109, 1982.

[66] D. H. Michael, "The separation of a viscous liquid at a straight edge," *Mathematika*, vol. 5, no. 1, pp. 82–84, 1958.

[67] H. K. Moffatt, "Viscous and resistive eddies near a sharp corner," *Journal of Fluid Mechanics*, vol. 18, no. 1, p. 1–18, 1964.

[68] G. C. Georgiou, L. G. Olson, W. W. Schultz, and S. Sagan, "A singular finite element for Stokes flow: The stick–slip problem," *International Journal for Numerical Methods in Fluids*, vol. 9, no. 11, pp. 1353–1367, 1989.

[69] G. C. Georgiou, W. W. Schultz, and L. G. Olson, *Singular Finite Elements for Fluid Flow Problems with Stress Singularities*, pp. 174–176. Dordrecht: Springer Netherlands, 1990.

[70] M. Elliotis, G. Georgiou, and C. Xenophontos, "Solution of the planar Newtonian stick–slip problem with the singular function boundary integral method," *International Journal for Numerical Methods in Fluids*, vol. 48, no. 9, pp. 1001–1021, 2005.

[71] T. R. Salamon, D. E. Bornside, R. C. Armstrong, and R. A. Brown, "Local similarity solutions for the stress field of an Oldroyd-B fluid in the partial-slip/slip flow," *Physics of Fluids*, vol. 9, no. 8, pp. 2191–2209, 1997.

[72] J. D. Evans, "Stick-slip and slip-stick singularities of the Phan-Thien–Tanner fluid," *Journal of Non-Newtonian Fluid Mechanics*, vol. 199, pp. 12 – 19, 2013.

[73] J. D. Evans, "Stick-slip singularity of the Giesekus fluid," *Journal of Non-Newtonian Fluid Mechanics*, vol. 222, pp. 24 – 33, 2015. Rheometry (and General Rheology): Festschrift dedicated to Professor K Walters FRS on the occasion of his 80th birthday.

[74] J. D. Evans, I. L. Palhares Junior, and C. M. Oishi, "Stresses of PTT, Giesekus, and Oldroyd-B fluids in a Newtonian velocity field near the stick-slip singularity," *Physics of Fluids*, vol. 29, no. 12, p. 121604, 2017.

[75] T. R. Salamon, D. E. Bornside, R. C. Armstrong, and R. A. Brown, "The role of surface tension in the dominant balance in the die swell singularity," *Physics of Fluids*, vol. 7, no. 10, pp. 2328–2344, 1995.

[76] H. Lugt and E. Schwiderski, "Flows around dihedral angles. i. eigenmotion analysis," *Proceedings of the Royal Society of London Series A*, vol. 285, no. 1402, pp. 382–399, 1965.

[77] E. J. Hinch, "The flow of an Oldroyd fluid around a sharp corner," *Journal of Non-Newtonian Fluid Mechanics*, vol. 50, no. 2, pp. 161 – 171, 1993.

[78] M. Renardy, "How to integrate the upper convected Maxwell (UCM) stresses near a singularity (and maybe elsewhere, too)," *Journal of Non-Newtonian Fluid Mechanics*, vol. 52, no. 1, pp. 91–95, 1994.

[79] J. M. Rallison and E. J. Hinch, "The flow of an Oldroyd fluid past a reentrant corner: The downstream boundary layer," *J. Non-Newtonian Fluid Mech*, vol. 116, pp. 141–162, 01 2004.

[80] M. Renardy, "The high Weissenberg number limit of the UCM model and the Euler equations," *Journal of Non-Newtonian Fluid Mechanics*, vol. 69, no. 2, pp. 293 – 301, 1997.

[81] F. Pimenta and M. A. Alves, "rheotool." https://github.com/fppimenta/rheoTool, 2016.

[82] S. S. Deshpande, L. Anumolu, and M. F. Trujillo, "Evaluating the performance of the two-phase flow solver interFoam," *Computational Science & Discovery*, vol. 5, p. 014016, nov 2012.